Development of Multi-perspective Diagnostics and Analysis Algorithms with Applications to Subsonic and Supersonic Combustors

Andrew Joseph Wickersham

Dissertation submitted to the faculty of the Virginia Polytechnic Institute and State University in partial fulfillment of the requirements for the degree of

Doctor of Philosophy
In
Mechanical Engineering

Co-chair: Lin Ma
Co-chair: Uri Vandsburger
Srinath V. Ekkad
Wing F. Ng
Kevin T. Lowe
Joseph A. Schetz

November 18, 2014
Blacksburg, Virginia, USA

Keywords: Combustion, Chemiluminescence, Proper Orthogonal Decomposition, Wavelet Transform

Development of Multi-perspective Diagnostics and Analysis Algorithms with Applications to Subsonic and Supersonic Combustors

Andrew Joseph Wickersham

Abstract

There are two critical research needs for the study of hydrocarbon combustion in high speed flows: 1) combustion diagnostics with adequate temporal and spatial resolution, and 2) mathematical techniques that can extract key information from large datasets. The goal of this work is to address these needs, respectively, by the use of high speed and multi-perspective chemiluminescence and advanced mathematical algorithms.

To obtain the measurements, this work explored the application of high speed chemiluminescence diagnostics and the use of fiber-based endoscopes (FBEs) for non-intrusive and multi-perspective chemiluminescence imaging up to 20 kHz. Non-intrusive and full-field imaging measurements provide a wealth of information for model validation and design optimization of propulsion systems. However, it is challenging to obtain such measurements due to various implementation difficulties such as optical access, thermal management, and equipment cost. This work therefore explores the application of FBEs for non-intrusive imaging to supersonic propulsion systems. The FBEs used in this work are demonstrated to overcome many of the aforementioned difficulties and provided datasets from multiple angular positions up to 20 kHz in a supersonic combustor. The combustor operated on ethylene fuel at Mach 2 with an inlet stagnation temperature and pressure of approximately 640 degrees Fahrenheit and 70 psia, respectively. The imaging measurements were obtained from eight perspectives

simultaneously, providing full-field datasets under such flow conditions for the first time, allowing the possibility of inferring multi-dimensional measurements.

Due to the high speed and multi-perspective nature, such new diagnostic capability generates a large volume of data and calls for analysis algorithms that can process the data and extract key physics effectively. To extract the key combustion dynamics from the measurements, three mathematical methods were investigated in this work: Fourier analysis, proper orthogonal decomposition (POD), and wavelet analysis (WA). These algorithms were first demonstrated and tested on imaging measurements obtained from one perspective in a sub-sonic combustor (up to Mach 0.2). The results show that these algorithms are effective in extracting the key physics from large datasets, including the characteristic frequencies of flow–flame interactions especially during transient processes such as lean blow off and ignition. After these relatively simple tests and demonstrations, these algorithms were applied to process the measurements obtained from multi-perspective in the supersonic combustor. compared to past analyses (which have been limited to data obtained from one perspective only), the availability of data at multiple perspective provide further insights into the flame and flow structures in high speed flows.

In summary, this work shows that high speed chemiluminescence is a simple yet powerful combustion diagnostic. Especially when combined with FBEs and the analyses algorithms described in this work, such diagnostics provide full-field imaging at high repetition rate in challenging flows. Based on such measurements, a wealth of information can be obtained from proper analysis algorithms, including characteristic

frequency, dominating flame modes, and even multi-dimensional flame and flow structures.

Acknowledgements

It is important for me to first and foremost acknowledge Dr. Lin Ma. Enough cannot be said about the support and guidance that he has given me throughout my tenure at Virginia Tech. As an advisor, professor, mentor and friend, Dr. Ma has shown and taught me more about all aspects of engineering and life than words can begin to describe. I would also like to thank Dr. Srinath Ekkad for selecting me out of many incoming graduate students when I first arrived at Virginia Tech to work on his project and for having confidence in me to succeed year after year when sometimes I was uncertain. I would also like to thank Dr. Uri Vandsburger for his dedication to maintaining a laboratory that fosters science and technology, where the bulk of this work was completed. Also, to my faculty committee and the many professors that challenged me throughout the years for their tireless dedication to my education; it made a difference in my life and definitely did not go unnoticed. One particular professor that deserves credit is Dr. Yitung Chen, for challenging me to succeed beyond what I thought was possible in the early years at UNLV.

Another sincere acknowledgement is in order for my fellow graduate students. In particular, two individuals stand above the rest: Dr. Ryan Blanchard and Dr. Xuesong Li. Dr. Ryan Blanchard was always there for me every step of the way with advice, research guidance, qualifier help, homework/project help, CFD mini-lectures, and so much more. To date, despite numerous attempts, I do not think there was ever a time that he was not able to answer a single one of my many, many questions. I truly hope someday that I can repay the shear time and dedication that he showed me during our stay at the CSDL. Dr.

Xuesong Li is a technical genius and without his tireless efforts during the first few years of my studies, I do not think I would have survived to this day. Also, to the many other students who helped make this possible, Cory Fleischman, Craig English, Dr. Jordan Farina, Sam Shiver, Yue Wu and Qingchun Lei, thank you for having the patience with me when I was new to full scale combustion experiments and for shaking me out of the monotony of graduate school life when I really needed it.

I would like to thank Rolls-Royce and the Air Force Research Laboratory for the financial support and facilities that made this work possible. Specifically, I would like to thank Dr. Duane Smith for his expert technical skills with our many experiments and for his personal advice with regards to my career path. To take time out of your busy schedule to discuss career decisions and life meant more to me than you realize.

Lastly, I cannot forget my loved ones. Dad, even though I now “outrank” you with education, you will still be the smartest man that I know. Mom, to say that you provided me with emotional support does not begin to put it into words. Jack and Matt, whether you believe me or not, I am constantly sprinting to catch up to the successes you two garner every day. You both constantly inspire me and I am extremely thankful to have older brothers like you. And last, but certainly not the least, to Kimberly Hammer, for your patience when 2 years turned into 4, enduring the extremely long distance of Nevada/Arizona to Virginia and for your never ending love and support when sometimes I am sure I did not deserve it.

To Henry Elias and Cooper Jeffrey, may this be a mark that you too surpass one day.

Table of Contents

List of Illustrations

List of Tables

Chapter 1. Introduction

1.1. Motivations

After continued research efforts, the ability to predict combustion processes accurately has remained inconclusive due to the multi-physics that occur and couple at multiple scales [1]. To develop predictive combustion models for the particular yet important issue of combustion instabilities, three basic issues need to be well understood. First, the frequency of oscillation needs to be known. Second, the conditional occurrence at which these oscillations will occur needs to be understood. Lastly, the amplitude of these oscillations needs to be predicted. There already exists reasonable frequency predictive capabilities, but the complexity of the flame regions in modern combustors renders the conditional occurrence of these dynamics difficult to predict [2]. Also, complicated combustor geometries and strict emission standards lead to flame structures that are still difficult to model and whose effect on instabilities is still under investigation [2].

To address these existing research issues, there have been intense investigations into numerical modeling of complex combustion flows to further understand the dynamics involved and how they behave over a variety of conditions [3, 4]. However, there is a critical need for experimental data with adequate temporal and spatial resolution to validate these model and computational results.

Previous and existing diagnostic have centered on low order (low sampling rate or small number of samples) and two-dimensional (2D) measurements, due to technological limitations and optical access in model and full scale experiments. However,

advancements in optics and camera technology now make it possible to image combustion flows at tens of kilohertz at full-scale resolutions through optical fibers, which offers the possibility of extending 2D measurements to multidimensional measurements. With the increase in temporal and spatial resolution, there is now a corresponding need for numerical schemes more than ever 1) to extract key physics from both the experimental and computational results, and 2) to compress these results to a low order representation, such that a comparison can be made between experiments and simulations to facilitate the model validation and model development processes.

Under the above context, the diagnostic methods and numerical algorithms demonstrated herein are developed to provide experimental data for the understanding of complex flame structures in representative combustion flows. These data are useful for the comparison to computational fluid dynamics (CFD) and large eddy simulation (LES) results.

1.2. Scope of the current work

The scope of the current work is to investigate the spatial heat release structures for subsonic and supersonic, partially premixed, hydrocarbon flames through the use of high speed chemiluminescence combined with numerical algorithms (proper orthogonal decomposition, Fourier transform, and continuous wavelet transform). The experiments described in this work were performed on a subsonic combustor representing a model afterburner and a supersonic combustor representing a scramjet. The large coherent structures derived from the POD analysis provide insight to the dominant modes inherent with these reacting flows, which will provide information on the spatial structure of the

heat release oscillations within these chemical reactions. Also, the weighted temporal coefficients associated with these modes provide insight to the dominant frequency at which these modes oscillate. Finally, the high speed chemiluminescence measurements and analytical methods are extended to multi-perspective measurements, so that the dominant spatial modes and their frequency from multiple perspectives can be studied.

1.3. Organization of the dissertation

The remainder of this dissertation is organized as follows.

Due to the multi-disciplinary nature of this work, Chapter 2 first summarizes the fundamentals of the major components relevant to this work. Chapter 2 continues by discussing the fundamentals of combustion instabilities and how they present themselves in subsonic combustors with a bluff-body flameholder and supersonic combustors with a cavity-based flameholder. Chapter 2 then discusses the theory behind combustion chemiluminescence to illustrate how it can be used as an effective diagnostic to quantify heat release in reactive flows. Lastly, Chapter 2 discusses the mathematical background of proper orthogonal decomposition and the continuous wavelet transform and how each can be leveraged to extract the most out of the aforementioned chemiluminescence measurements.

Chapter 3 reports the results obtained on the subsonic combustor with a vee-gutter flameholder. The experiments were performed at Virginia Tech's Combustion Systems Dynamics Laboratory (CSDL). These experiments demonstrated the method's ability to extract the correct coherent structures from different operating conditions and

demonstrated the differences in frequency and spatial structure observed as a function of operating condition.

Chapter 4 reports the results obtained on the supersonic combustor with a cavity-based flameholder. The experiments were performed in a supersonic wind tunnel housed in Research Cell 19 at Wright-Patterson Air Force Base. These experiments extended the previous single perspective measurements to multiple perspectives, and results obtained also as a function of operating conditions were analyzed and reported. The results demonstrated the similarities and differences observed in the spatial heat release structures and frequency as a function of location and perspective.

Chapter 5 provides concluding remarks to the work described in this dissertation and makes recommendations for future research.

Chapter 2. Background

2.1 Combustion instabilities

Combustors of all kinds experience various degrees of dynamics or instabilities. Chemical energy is converted into sensible heat during the combustion processes, which also produces dilatation in the working fluid. This dilatation produces local acceleration, which generates local pressure oscillations that can couple with the acoustical field within the combustion chamber. This can create a self-excited feedback loop that can subsequently lead to thermo-acoustic instabilities. These instabilities represent significant issues in the design and operation of combustors. They can decrease combustion efficiency, increase the production of pollutants, and in extreme cases, lead to total combustor failure [1].

Studies have been performed to identify and describe the driving mechanisms of these combustion instabilities and be able to passively or actively control them to within tolerable levels. It is well documented that the formation and convection of coherent large-scale structures caused by inlet velocity perturbations play a critical role in inducing these oscillations [5-7]. Another important mechanism is the temporal and/or spatial variations of fuel-air ratio caused by the propagation of pressure waves from the combustion chamber to the mixing section, where local flow non-uniformities occur. This non-uniformity generates temporal and/or spatial heat release perturbations that impinge on the flame [8-10]. Cho and Lieuwen [11] have performed a complete analysis of these major heat release fluctuation sources as shown in Figure 2.1.

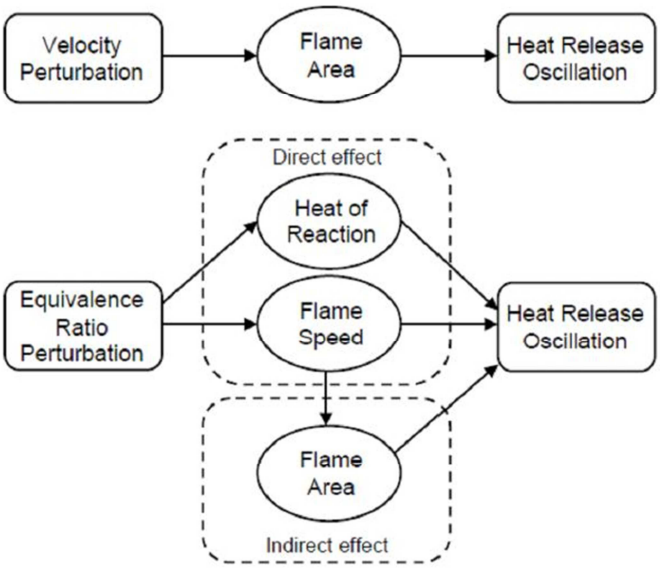

Figure 2.1. Dominant processes generating heat release oscillations caused by acoustic velocity perturbation (u') and equivalence ratio perturbation (q') [11].

As indicated in Figure 2.1, a major component of heat release oscillations is the spatial distribution of the flame area. Most recently, this indirect effect of equivalence ratio has been researched and shown to have a profound effect on the phase and frequency of the thermo-acoustic instabilities [12]. It is this feature of flame area or structure that will be examined closely in this work via chemiluminescence emitted by CH* radicals from multiple perspectives. High speed imaging measurements up to 20 kHz have been performed in both subsonic and supersonic combustors as to be described in the upcoming sections.

2.2. Flameholding in subsonic flows

A primary requirement for combustion in high speed flows (such as in gas turbine combustors) is to ensure that combustion is maintained over a certain range of operating

conditions. This requirement is especially critical for flight applications, both due to the catastrophic consequence of combustion instabilities and also due to the complexity of their operating conditions. The operating conditions vary in terms of pressures, temperatures, and also equivalence ratios. The equivalence ratios sometimes can fall outside the normal flammability limits for hydrocarbon and air mixtures. It is challenging to maintain stability under all these varying conditions in a high speed environment, as chemical reactions must be initiated and sustained when the flow speed may exceed the flame speeds by a large margin.

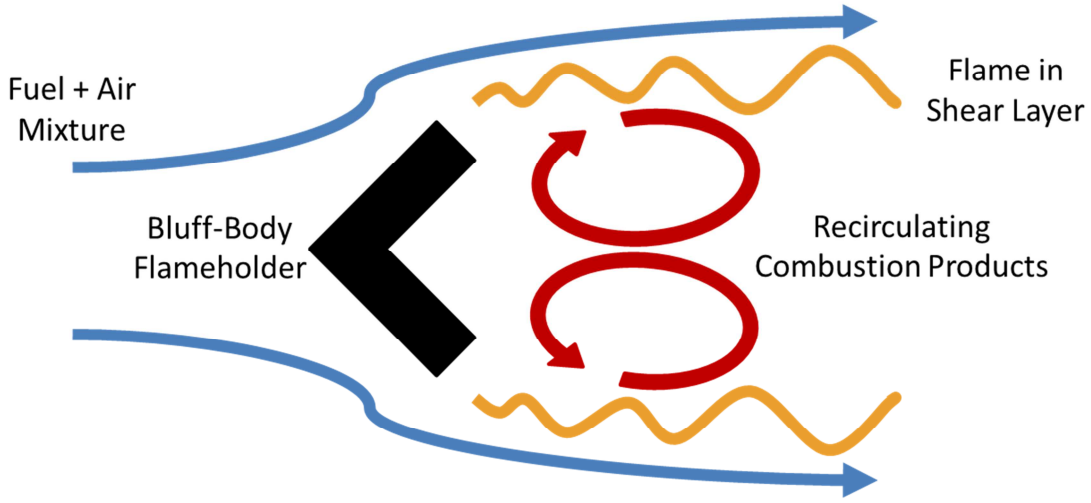

Figure 2.2. Schematic of a vee-gutter stabilized turbulent premixed flame showing the recirculation of combustion products from the bluff-body's wake into the shear layer [13]

The usual method of stabilizing the combustion in a high speed flow is to use a flameholder as shown in Figure 2.2 to create a sheltered zone of low velocity upstream of the reaction zone, which allows a relatively longer residence time chemical reaction to occur behind the flameholder. As shown, this also generates a recirculating region or regions that allow the hot combustion products to mix with the incoming air and fuel to

facilitate combustion. One particular example of creating this sheltered zone with subsonic combustion is the use of bluff-body flameholders. Various designs have been employed and studied experimentally, from flat plates [14, 15], to rods [16-19], to spheres [20] or cylinders [21], to vee-gutters [21-24] as shown in Figure 2.2. It is the focus of this work to examine a vee-gutter flameholder, which represents a fundamental configuration and is also found in extensive applications in practice.

Several different researchers have numerically and experimentally examined the behavior of vee-gutter-type combustion. Macquisten and Dowling [25] experimentally measured low-frequency combustion oscillations in a model afterburner using pressure transducers and a photo-multiplier tube (PMT) filtered to observe C_2 chemiluminescence for Mach 0.15-0.27 flows. They observed an increase in characteristic frequency with increasing inlet temperature and Mach number. Schuller et. al. [26] examined the laminar flame transfer function for V-flame dynamics using a combination of particle image velocimetry, CH* chemiluminescence, and laser Doppler velocimetry diagnostics. They observed the V-flame behaves as an amplifier in a certain range of frequencies and that this behavior is largely dependent on the flame angle. They also found a relationship between an increasing flame angle and a reduced gain in the flame transfer function, which relates to an increase in stability with increasing flame angle. Kato et. al. [27] took this a step further and expanded the one-dimensional, fixed, linear flame model to a spatially oscillating, one-dimensional model where the flame was not confined to a fixed plane, but was allowed to oscillate in a triangular predetermined zone. Their results showed a clear influence numerically and experimentally of flame shape/area on the oscillatory frequency of the combustion instabilities. Cho et. al. [11] also confirmed that,

for a non-vee-gutter geometry, the flame area was an indirect effect of equivalence ratio perturbations and played a role with heat release oscillations. Santosh et. al. [28] built upon the aforementioned work of Cho et. al. and expanded the analysis into the non-linear regime. Santosh's [28] work resulted to one critical finding that leads to heat-release saturation, which is a flame-kinematic mechanism. This mechanism arises due to fluctuations in flame position associated with the oscillations in flame speed [28]. Emerson et. al. [18], recognizing that large scale structures play important roles in vee-gutter combustion instabilities, decided to experimentally characterize the role of flame density ratios on vee-gutter wakes. They found the bluff-body wake was a strong function of density ratio, but that no sharp bifurcation occurs with variations of the ratio between the unburned density and burned density [18]. More recently, Kheirkhah et. al. [16] simplified their experiment to a benchtop type flame to experimentally analyze the flame-front characteristics of a turbulent, premixed, V-shaped flame using Mie-scattering and particle image velocimetry techniques. Ultimately, they found for all experimental conditions tested, large turbulent structures played a significant role in the wrinkling of the flame front. Allison et. al. [12] studied a well understood combustion instability on the DLR Stuttgart, dual-swirl, model combustor by varying the air velocity, flame speed and flame shape. They used high-speed CH_2O planar laser induced fluorescence (PLIF) to study the motion of flame surfaces in response to pressure oscillations. Their results show that the flame surface density fluctuated at the acoustic frequency of 320 Hz. They also showed that flame shape plays an important role with combustion instabilities by their comparison of flat flames to V-shaped flames. From their PLIF measurements, they observed a larger flame surface area and that the peak flame surface density was located

at larger radial distances for the resonating case versus the non-resonating case. But, the flame surface also exhibited asymmetric motions at 525 Hz associated with the presence of the PVC. Lastly, they postulated that the flame geometry, including its spatial and temporal variations, could be more accurately determined using kHz PLIF rather than by conventional chemiluminescence.

From this evolution of studies, it is clear that flame geometry and *spatial* variations of the heat release play a critical role in the understanding of bluff-body combustion and its instabilities. Therefore, it is the goal of this work to build upon the previous works and analyze the large coherent structures that dominate the unsteady heat release using various numerical methods. It is also the goal of this work to characterize the oscillatory behavior of these dominant modes via a continuous wavelet transform to observe the dynamic time-frequency dependence of these structures. Finally, this work will perform the analysis using high-speed chemiluminescence obtained from multiple perspectives to compare and contrast their effects on the heat-release dynamics of the system.

2.3. Flameholding in supersonic flows

Cavity-based flameholders are commonly used for hydrocarbon-fueled, supersonic, ramjet (scramjet) combustors [29]. This is due to the formation of a recirculation zone with a longer fluid mechanical residence time than the core flow of the duct. This enables relatively longer residence time chemical reactions to occur within the cavity [30]. These types of combustors have previously been demonstrated as a suitable option for dual-mode scramjet flameholding [31, 32]. Several variables have been

investigated with regards to cavity-based flameholders such as fuel mixing and rich/lean blowoff [33, 34], pressure/acoustic oscillations and shock propagation [29, 35-37], qualitative effects of heat release [30, 38], fuel injection strategies [30, 33, 39, 40] and velocity field and shear-layer interaction [41, 42]. There have also been attempts to numerically simulate this combustion geometry to better understand the cavity effect on mixing, total pressure loss and combustion efficiency [43, 44]. Through these works, geometries containing a downstream ramp with direct cavity fuel injections from the ramp produced the best fuel mixing and most robust combustion at a variety of inlet conditions [30]. A number of experiments have confirmed this finding via planar-laser induced fluorescence (PLIF) of *OH*, CH_2O radicals and *NO* [30, 32] and flame chemiluminescence imaging of electro-magnetically excited *OH (OH*)* and *CH (CH*)* radicals [30]. However, all reports observed large-scale, three-dimensional or out-of-plane features in the reacting cavity [32, 33] or localized emission structures that correlate to flame unsteadiness [30]. This results in the physical mechanism of flameholding and the flame structure not being well-understood [42]. Therefore, it is the goal of this work to expand upon the aforementioned studies and attempt to characterize the dominant flame structure and oscillatory modes inherent with cavity-based combustors at fuel-lean and fuel-rich conditions, by imaging the chemiluminescence from a variety a viewing angles simultaneously.

2.4. Chemiluminescence

Chemiluminescence is defined as the spontaneous electromagnetic radiation that is emitted when a chemically excited molecule is de-excited to its lower energy or ground

state [45]. Each radiating molecule emits energy at a characteristic wavelength, which depends upon the structure of the molecule and the transition process that the molecule undergoes.

This chemiluminescence process can be well explained using the laws of quantum mechanics. The chemiluminescence species can be molecules, atoms, ions, or even free electrons. For the simplicity of discussion, all these possible chemiluminescence species are collectively referred to as particles. These particles can have various energy levels associated with them. From a quantum mechanics point of view, a photon is the basic unit of radiative energy; therefore, radiative emission is defined as the release of photons or photonic energy. When a photon is emitted or absorbed, the energy of the emitting or absorbing particle is correspondingly decreased or increased. The magnitude of energy transition is related to the frequency of the emitted or absorbed radiation. The energy of the photon is physically defined as the product of Planck's constant, h and the frequency of the photonic energy, ν. Thus, for energy de-excitation or transition from an excited state (E_1) to the ground state (E_0), a photon is emitted with energy given by

$$E_2 - E_1 = h\nu \tag{2.1}$$

The frequency of the emitted energy is therefore defined as:

$$\nu = \frac{E_2 - E_1}{h} \tag{2.2}$$

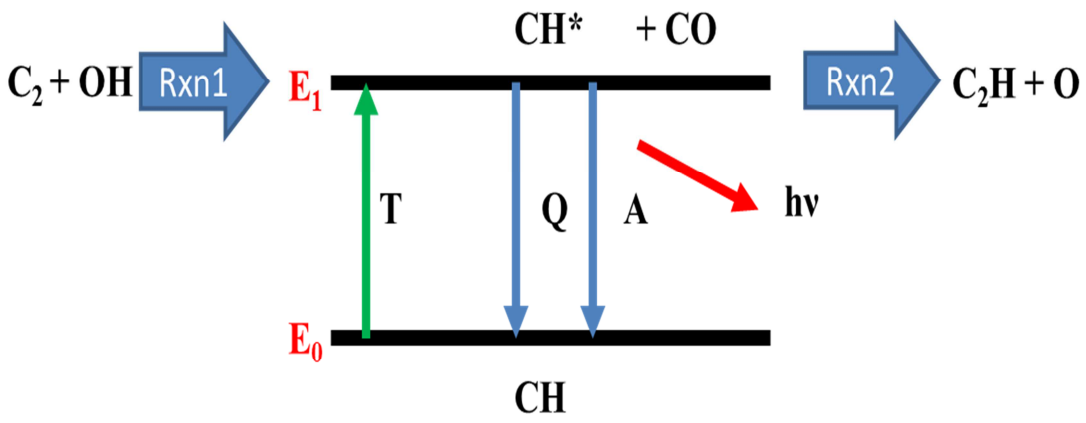

Figure 2.3. Fundamental processes involved in chemiluminescence measurements.

These absorption and excitation processes are shown in Figure 2.3. First, the excited state is formed via chemical reaction through thermal excitation. Then the de-excitation process can proceed in three possible ways: collisional quenching, spontaneous emission, and/or a reactive collision with another molecule. Often the de-excitation process is dominated by collisional quenching under typical combustion conditions, with the process limited by the formation of the excited state [46]. It is for this reason that the mechanism can be assumed to be in a quasi-steady state and a differential equation can be derived for the concentration of the excited species in question, as shown below [47].

$$\frac{d[CH^*]}{dt} \approx 0 = Rxn1 + T - Q - A - Rxn2 \qquad (2.3)$$

The emitted frequency or chemiluminescence signal emitted by this process is important because it can be correlated to the de-excitation of certain species of interest in combustion reactions. These dominant species can then be associated with the chemical equations that make up the dominant heat release in the hydrocarbon and air combustion systems. The common species of interest for combustion chemiluminescence are *OH**, *CH**, C_2*, and CO_2*, which emit mainly in the ultra-violet (UV) or visible (VIS)

spectrum and can be readily captured with standard or intensified high speed cameras [45]. By studying the light emission from these species, some insight can be gained about the energy release in the reaction zone of the flame that relate to combustor performance, pollutant formation and combustor health.

The adequacy of chemiluminescence as a combustion diagnostic for heat release has been debated for decades. Much of the research to date has been performed on controlled laboratory experiments that precisely vary equivalence ratio, curvature, strain rate, reactant combinations, pressure and inlet temperature to determine relationships between these quantities and chemiluminescence signals. These relationships are important when concerned with the robustness or accuracy of the measurement; therefore, it is important to analyze each chemiluminescence relationship and to choose the best indicator of heat release.

It is widely agreed that C_2* chemiluminescence is an inadequate indicator of heat release in the combustion reaction zone, as it not spatially correlated with heat release and is not associated with the major energy releasing reaction path for hydrocarbon flames [48-51].

Other studies have shown that CO_2* emission could be considered a good indicator of total or integrated heat release or even local heat release for low turbulence flames [51]. For example, Samaneigo et al. [47] showed that CO_2* chemiluminescence intensities vary monotonically with most flame properties, but not uniquely.

The most common chemiluminescence signals measured with gaseous and liquid fueled combustion are emitted from OH* and CH* radicals, not only as a heat release indicator, but also to indicate several flame properties such as equivalence ratio and

temperature [52-56]. Lee and Santavicca [9] used these measurements to classify the flame's structure during unstable combustion when combined with phase-synchronized pressure measurements. Other studies, however, observed that OH* chemiluminescence in turbulent flames and flames with high strain rates reported poor agreement with heat release, in that the emission varied strongly with turbulence level and even disappeared at high strain rates [50, 51, 57-59]. Also, at elevated pressures, it has been shown computationally that thermal excitation of OH molecules is the primary source of OH* radicals rather than the expected chemical excitation that would be associated with the heat generating reaction path [60]. However, CH* chemiluminescence does not succumb to this limitation because it has been shown that a quasi-steady state assumption for CH* production can be assumed reasonably, as CH* radicals are largely chemically excited and dominated by quenching. It is for this reason that CH* is often used in gas turbine combustor experiments. For example, Lieuwen and Neumeier [61] and Bloxsidge et al. [62] have reported on the use of CH* to obtain transfer functions relating heat release and pressure fluctuations in an unsteady combustor.

This work primarily focused on CH* emission due its robustness in high strain environments and its relatively higher signal levels in the visible spectrum compared to OH*. The chemiluminescence emission from CH* is due to $A^2\Delta \rightarrow X^2\Pi$ (~431 nm) and $B^2\Sigma^- \rightarrow X^2\Pi$ (~390 nm) transitions, with the former usually dominating [45]. Of the various proposed sources for CH*, research has focused on the following three reaction mechanisms:

$$C_2 + OH \rightarrow CH^* + CO \qquad \text{(R1)}$$

$$C_2H + O \rightarrow CH^* + CO \qquad \text{(R2)}$$

$$C_2H + O_2 \rightarrow CH^* + CO_2 \qquad \text{(R3)}$$

Radiative rates and quenching data for these mechanisms for major hydrocarbon species are available in the literature [63, 64]. Extensive research has been completed with regards to these mechanisms and is summarized in Nori [46]. An example of this is in a recent shock tube study with methane-hydrogen mixtures, which supports R1 and R2 as the dominant CH* formation pathways for conditions in the range of 1200-2300 K and 0.6-2.2 atm, though with large uncertainties in the rate parameters due to inadequate information on C_2 kinetics [65].

It is worth noting that chemiluminescence by nature is a line-of-sight or path integrated measurement. This can include optical distortions from the transparent combustor windows and/or a reduction in observable detail in the flame. In the past, this has been a limitation of chemiluminescence for a valid comparison to computation fluid dynamic (CFD) models. However, it is the purpose of this thesis to expand upon this limitation by imaging high speed CH* chemiluminescence emission from multiple perspectives to analyze the spatial structure of the heat release in a model scramjet combustor. This will add significant value to CH* chemiluminescence measurements in gas turbine combustors for the reasons listed previously with the addition of capturing the spatial structure of this heat release simultaneously from multiple views.

2.5. Proper orthogonal decomposition

Due to the high speed and multiple perspective nature of the measurements, the chemiluminescence data captured in this thesis were on the order of tens of tera-bytes (TBs), with measurements for each individual test condition consisting of several

thousand images or tens of giga-bytes (GBs) of data. In order to analyze the physics involved with the spatial heat release structures for each test and be able to compare results across conditions, a robust and systematic method needed to be used to compress such large data sets down to a lower order approximation representing the dominant variance of each system. This method also needed to replace the usual Fourier decomposition to be able to handle non-homogeneous or non-periodic directions. A very effective method to accomplish these goals was a type of modal decomposition termed the proper orthogonal decomposition (POD).

POD was first introduced by Lumley in the context of turbulence as an objective definition to a periodic phenomenon now widely known as coherent structures [66]. These coherent structures appear to be dynamically important and play a key role in determining the macro-characteristics of flow fields such as mass, momentum, energy and heat transports, combustion entrainment in shear layers, chemical reactions, drag and aerodynamic noise generation [67]. Since Lumley, POD has been reintroduced with the application to a variety of fields by Kosambi [68], Karhunen [69], Loève [70], and Sirovich [71]. As a result, this technique is often referred to by different names based on the discipline. The most common names associated with POD are the Karhunen-Loève expansion, Principal Component or Hotelling Analysis, and Singular Value Decomposition. Despite the names, the principles are the same in that the method yields a reduced set of basis functions, and these basis functions are optimal in the sense that no other decomposition technique of equal order captures an equivalent amount of kinetic energy.

Mathematically, the basic idea of POD is to describe a given statistical ensemble with the minimum number of deterministic modes. To simplify the process, let $u(s)$ be a random scalar field defined on a real-line interval, where s is defined as a spatial and/or temporal parameter. We would like to find a deterministic function that is most similar to the ensemble mean. To accomplish this, one way is to maximize the projection of $u(s)$ onto the deterministic function, which we will call $\phi(s)$. Mathematically, this process corresponds to seeking a function that needs to be maximized, such that,

$$\frac{\langle|(u,\phi)|^2\rangle}{(\phi,\phi)} = \lambda \geq 0 \tag{2.4}$$

That is, we determine the component of ϕ, which maximizes the normalized inner product with the scalar field u. This represents a classical problem in the calculus of variations with a restriction that ϕ is an eigenfunction of the two-point correlation tensor [72],

$$\int R(s,s')\phi(s')ds' = \lambda\phi(s) \tag{2.5}$$

where $R(s,s') = \langle u(s)u^*(s')\rangle$ is an integratable, cross-correlation, Hermitian matrix or tensor between points s and s' and the asterisk (*) represents the complex conjugate. The solution to (2.5) forms a complete sequence of square-integratable, orthonormal eigenfunctions, $\phi_k(s)$ with associated eigenvalues, λ_k, normalized such that $\|\phi_k\| = 1$. If the eigenvalues are sorted by order such that $\lambda_i \geq \lambda_{i+1}$, observing that the non-negative mean $R(s,s')$ assures that $\lambda_i \geq 0$, we also have a diagonal decomposition [72],

$$R(s,s') = \sum_k \lambda_k \phi_k(s)\phi_k^*(s') \tag{2.6}$$

Knowing almost every member in an ensemble of random generalized functions can be represented by an infinite series of orthonormal functions with random, uncorrelated coefficients, the modal decomposition of the eigenfunctions becomes,

$$u(s) = \sum_k a_k \phi_k(s) \tag{2.7}$$

The diagonal representation of the $R(s, s')$ ensures that the modal amplitudes are uncorrelated by,

$$\langle a_k a_{k'}^* \rangle = \delta_{kk'} \lambda_k \tag{2.8}$$

Thus, the eigenvalues, λ provide the energy content of the various eigenfunctions or modes. Also, the formation of these modes involved the maximizing of the eigenvalues (or physically the relative energy per mode); therefore, the series (2.7) converges as rapidly as possible. In result, the final product is an optimal set of basis functions in terms of energy convergence.

Moreover, if the averaging takes place in the time domain, then $u(x, y, t)$, where *(x,y)* and *t* are space and time coordinates, can be represented by the following,

$$u(x, y, t) = \sum_k a_k(t) \phi_k(x, y) \tag{2.9}$$

where $a_k(t)$ are temporal coefficients and $\phi_k(x, y)$ are spatial eigenmodes.

The aim of this synopsis is not to present a complete derivation of POD with all mathematical evidences, but simply to derive the basic concepts of the decomposition technique to the reader. A more rigorous mathematical description of the POD transformation can be found in Berkooz et al. [72] or Laurent and Gilles [73].

The above approach outlines the general or classical framework of POD; however this method becomes increasingly more difficult computationally with an increasing number of spatial points. Therefore, Sirovich proposed that the temporal correlation matrix will yield the same dominant spatial modes, while often giving rise to a much smaller and computationally more tractable eigenproblem [71]. Hence a new method of POD for substantially larger spatial systems was developed, dubbed the *method of*

snapshots. Mathematically speaking, for the same process $u(x, y, t)$, instead of finding a spatial two-point correlation matrix, where *N* is the number of spatial variables, and solving (2.2), the computation of a temporal correlation (or covariance) matrix,

$$\mathbf{A}= \frac{1}{M}\int\int u(x,y,t_m)u(x,y,t_n)dxdy \tag{2.10}$$

can be completed, where *M* is the number of snapshots. The eigenmodes can then be represented as

$$\phi_k(x,y) = \sum_{i=1}^{M} b_i u_i(x,y) \tag{2.11}$$

where $\boldsymbol{b_i}$ is the solution to the generic eigenvalue problem

$$\boldsymbol{Ab} = \lambda \boldsymbol{b} \tag{2.12}$$

Thus, the cross-correlation degenerates into an auto-correlation, greatly simplifying the computational time and the series resembles the same solution as outlined in (2.9)

This *method of snapshots* is normally strictly employed under two common restrictions. 1). When the time division between subsequent snapshots is continuous and uniform. 2). When $M \ll N$, or the number of snapshots is much less than the number of spatial variables. For the experimental conditions employed in this dissertation, a high speed camera was used with a uniform time step between successive images, which satisfied condition 1. And, the images were on the resolution order of no less than 400 x 600 pixels (yielding 240,000 spatial variables) with series lengths of no more than 10,000 photos (or snapshots). Therefore, the number of snapshots is clearly much less than the number of spatial variables, which satisfies condition 2.

Before applying POD to any statistical data set, the user must understand the limitations of such technique and what the results physically mean, assuming the user intends to derive physical conclusions from the data set. Due to the temporal correlation

and integration over space during the POD transformation, the obtained results are often arguable to in fact be physical or real flow structures [74-76]. Regert et al [76] completed a simple, yet extremely valuable analysis of POD on synthetic flow fields. Regert determined that when the dataset did not contain any overlapping structures (i.e., the structures are separated in time only), then the POD analysis yielded as many dominant modes as there were non-overlapping structures. The number of dominant modes is determined by a dramatic drop in relative energy per eigenmode as shown in Figure 2.4

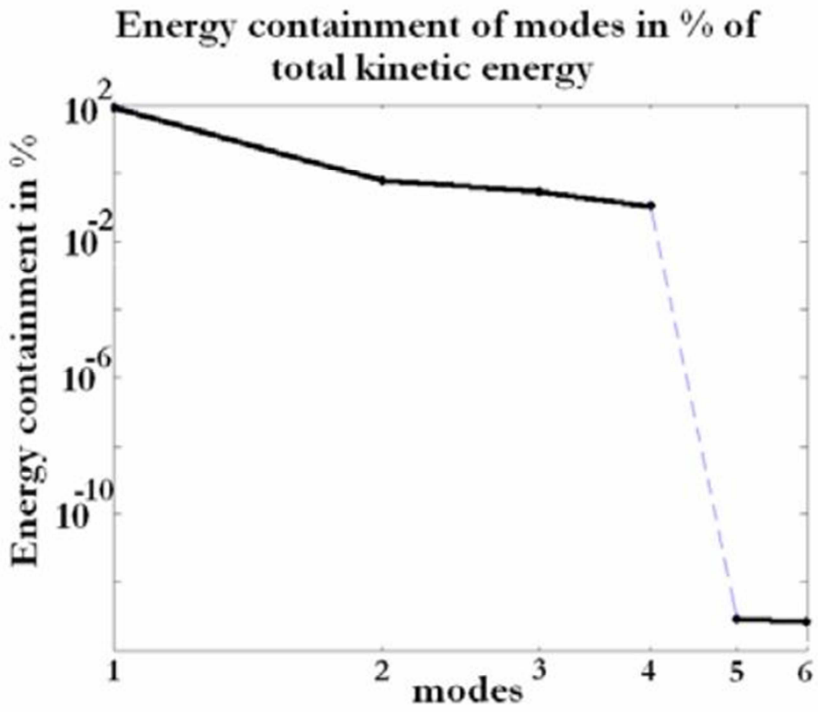

Figure 2.4. Mode energy content associated with data of non-overlapping vortex positions [76].

Regert also noted that when overlapping positions were present then the decomposition included some mathematical structures not existing in the original synthetic dataset. However, these "non-physical" modes were observed to also exist after

the sudden modal energy drop off point. Therefore, as a general conclusion, only modes with dominant relative energies can be considered physical. Regert further proved this by applying POD to a flow field over an open, rectangular cavity. Modes 1-3 showed a higher energy content than the remaining modes, and comparison to simulations showed physical similarities to the mean (because a mean subtraction was not performed in this work) and large scale, dominant or coherent structures.

This entire formulation was derived under the context of coherent structures as they pertain to turbulence, but it can also be applied to other forms of data as well. A complete literature search also found applications for POD in vibrations [77], detection and pattern recognition [78] to name a few, but most recently (within the past 5 years), it has been applied to combustion research. Combustion instabilities exhibit periodic fluctuations in heat release, which can be visualized using POD to gain better understanding of their structure and performance. POD was applied by Boxx et al. [79], Steinberg et al. [80] and Stohr et al. [81] to kHz rate particle image velocimetry data in Deutsches Zentrum fur Luft-und Raumfahrt's (DLR) model, swirl stabilized combustor to better characterize the nature of the fluid-dynamic phenomena responsible for the peaks in the power spectra. Boxx et al. [79] transformed the dominant eigenmode temporal coefficients with a Fourier transform and confirmed that the characteristic frequencies observed corresponded to the same characteristic flow structure observed in the combustor and thermo-acoustic frequencies measured via pressure transducers. Steinberg et al. [80] also transformed the dominant temporal coefficients with a Fourier transform and compared these characteristic frequencies with an intensity-weighted centroid analysis, which yielded similar results. POD combined with an a-posteriori

phase averaging procedure was applied to both confined and unconfined flames on a Triple Annular Research Swirler (TARS) to visualize the flame vorticity dynamics and azimuthal modes [82]. Most recently POD has been applied to broadband chemiluminescence data from a natural gas powered gas turbine burner [83], CH* chemiluminescence on different bluff-body combustion models [84], and OH-PLIF of a jet flame in a vitiated swirling crossflow [85]. All have proved POD useful in characterizing some of the dominant flow structures in the reaction zone and corresponding relationships between the dominant mode, temporal coefficients, characteristic frequencies and the thermo-acoustic oscillations within each system.

It is the goal of this work to build upon the aforementioned work and apply POD to CH* chemiluminescence from a subsonic vee-gutter combustor to characterize the differences and similarities in characteristic frequencies as a function of inlet Mach number. Also, to apply POD to CH* chemiluminescence from a model scramjet combustor to characterize the differences and similarities in characteristic frequencies as a function of fuel flow rates.

2.6. Continuous wavelet transform

The wavelet transformation is used to divide a continuous-time function into wavelets. The purposes of these wavelets are to construct a time-frequency representation of the signal that offers time and frequency localization rather than a global frequency approximation of the entire temporal domain like a Fourier transformation.

The continuous wavelet transform (CWT) of a signal $f(t) \in L^2(\boldsymbol{R})$ is defined as the inner product in the Hilbert space of the L^2 norm as follows,

$$M(a,b)\{f(t)\} = \frac{1}{\sqrt{a}}\int_{-\infty}^{+\infty} f(t)\Psi_{\mathrm{a,b}}^{*}dt \tag{2.13}$$

where

$$\Psi_{a,b} = \frac{1}{\sqrt{a}}\Psi\left(\frac{t-b}{a}\right) \tag{2.14}$$

and b is called the shift parameter, which provides the temporal information, a is the scaling or dilatation parameter, which is inversely related to frequency, $\frac{1}{\sqrt{a}}$ is used to ensure energy preservation and $\Psi_{\mathrm{a,b}}$ is called the mother wavelet (* denotes complex conjugate), which is selected based on what type of information is desired from the data set analyzed. If a is small, then higher frequency components can be analyzed, versus when it is larger, lower frequency components can be examined. When b is a fixed value, the fundamental function can be shifted the distance b in the direction in which time advances. Mathematically if the wavelet $\Psi(t) \in L^2(R)$ and its Fourier transformation, $\widehat{\Psi}(f)$, satisfies the admissibility condition

$$C_{\Psi} = \int_{-\infty}^{+\infty} \frac{|\widehat{\Psi}(f)|^2}{|f|} df < \infty \tag{2.15}$$

$$\int_{-\infty}^{+\infty} \Psi(t) = 0 \tag{2.16}$$

where C_{Ψ} is called the wavelet admissible constant and *f(t)* is a continuous function, then this guarantees the existence of the inverse wavelet transformation.

$$m(t) = C_{\Psi}^{-1}\int_{-\infty}^{+\infty}\int_{-\infty}^{+\infty}\frac{1}{a^2}M(a,b)\Psi\left(\frac{t-b}{a}\right)dbda \tag{2.17}$$

For a discrete sequence u_m, let $t = m\delta t$ and $b = n\delta t$, where $m, n = 0,1,2,\ldots,N-1,N$, is the sampling point number and δt is the sampling interval. The CWT of u_m is defined as the following [86],

$$W_n(x_j) = \sum_{m=0}^{N-1} u_m \Psi^{*}\left[\frac{(m-n)\delta t}{x_j}\right] \tag{2.18}$$

If the index *j* and *n*, which correspond to the shift and scale parameters respectively, are varied, one can construct a relationship of the amplitude of any characteristic features versus their scale and how this amplitude varies with time. In general, wavelets can be classified into asymmetrical and symmetrical wavelets and depending on the application, a particular wavelet basis must be selected that is suitable for the purpose. The two most commonly chosen wavelet bases are the Morlet wavelet and the Mexican Hat wavelet. In this study the Morlet wavelet is used because it is closely related to human perception of acoustical measurements. It is defined as follows:

$$\Psi(t) = \pi^{-\frac{1}{4}} e^{iw_1 t} e^{-\frac{t^2}{2}} \tag{2.19}$$

where w_1 is the non-dimensional frequency. The function of a Morlet wavelet is an exponentially sinusoidal signal; therefore, its shape can be adjusted in order to adapt to the various sinusoidal waveforms that are commonly found in many dynamic or acoustic systems.

To illustrate the CWT and its usefulness in analyzing non-harmonic, non-linear, and transient signals, Figure 2.5 shows two example spectrograms of a linear and nonlinear chirp, defined in (2.20) and (2.21), respectively, below:

$$M_1(t) = t * \sin(2\pi t^2) \tag{2.20}$$

$$M_2(t) = \mathrm{e}^{3t} \sin(2\pi t * 50t^2) \tag{2.21}$$

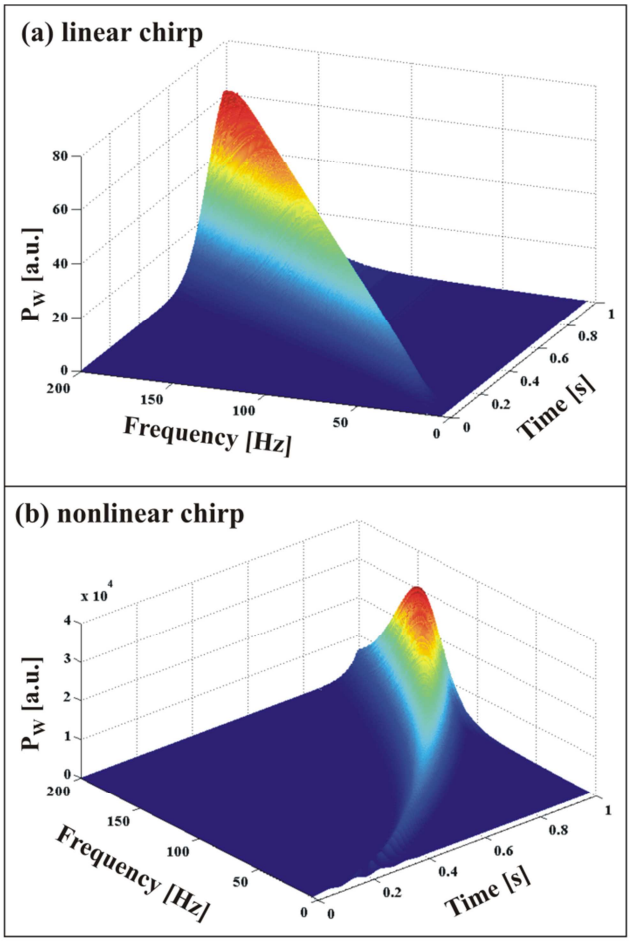

Figure 2.5. Panel (a) Power spectrum of a linear chirp. Panel (b) Power spectrum of a nonlinear chirp.

From the definition in (2.20) and (2.21), it is apparent that the linear chirp's frequency and magnitude both increase linearly with time, and the nonlinear chirp's frequency and magnitude (i.e., energy) both increase nonlinearly. The spectrograms in Panel (a) and (b) in Figure 2.5 obtained from the CWT, captures such transient features, elucidating both the dominating frequency components and how these components vary in time. Regular Fourier analysis is not able to capture such features in the signal (because it is performed over the entire time domain). A windowed Fourier transform (WFT), i.e., performing a Fourier analysis consecutively on segments of the target signal of length Δt, seems to be a

natural idea of extending the Fourier transform to transient signals [87]. However, the WFT extension has been shown to be both inaccurate and inefficient [87]. For example, the WFT method imposes an empirical scale (Δt) into the analysis and is therefore subject to the aliasing of low and high frequency components that are not contained in the windowed segment [87]. Many combustion processes are transient and feature a wide range of frequency components, which are unknown *a priori*. Therefore, the WFT method is unsuitable and a method that does not depend on the length of the windowed segment is desired.

The CWT or WA method overcomes the restrictions of the Fourier method by the careful choice of the basis functions. The wavelet basis functions are both localized in frequency (like the sines and cosines in a Fourier transform) and also in space (unlike the sines and cosines in a Fourier transform), enabling the time-frequency localization without the need of imposing Δt.

In fluid mechanics, the CWT was first used in the early 1990s to analyze turbulent flows [88]. Wavelet methods have also been developed for most kinds of linear partial differentiation equations (PDEs), such as Laplace/Poisson equations and heat and transport equations [89, 90]. Multi-resolution wavelet schemes, especially in the context of compressible Euler equations have been intensively studied in recent years [91, 92]. Wavelet methods in computational fluid dynamics (CFD) have only been a recent area of study in the past 15 years to more accurately define non-periodic boundary conditions to isolate and identify localized structures such as shock waves and vortices [93]. An excellent review of wavelet methods and their applications to CFD is available in Schneider and Vasilyev [89] for more information.

In combustion specifically, the CWT has been extensively used for fault or knock signal diagnosis and cycle-to-cycle pressure variations in internal combustion (IC) engines [86, 94]. For example, Sen et al. [94] found from the wavelet power spectrum, the presence of long, intermediate and short-term periodicities in the pressure signal. Also, that depending on the load, the periodicities appeared intermittently or spanned several cycles; therefore, knowledge of the periodicities proved useful in developing effective control strategies.

Other applications of the CWT has been with fringe analysis in optics by Wang et al [95] and in the use of a wavelet variant to correlate near-field pressure fluctuations to velocity modes in a supersonic jet [96]. More specifically Kastner et al. [97] used a Wavelet Stochastic Estimation scheme to extract frequency information from the pressure field of an over-expanded, supersonic, axisymmetric jet and then correlated the selected frequencies to the velocity measurements made with particle image velocimetry (PIV).

It is the goal of this work to build upon the previous work and apply the CWT to POD results of CH* chemiluminescence from a model, subsonic, vee-gutter combustor to characterize the differences and similarities in characteristic frequencies as a function of inlet Mach number. Also, to apply the same numerical scheme to CH* chemiluminescence from a model scramjet combustor to characterize the differences and similarities in characteristic frequencies as a function of fuel flow rates.

Chapter 3. Measurements and analysis of subsonic combustion flows

3.1. Experimental operating conditions

The subsonic experiments were conducted in a combustor housed in the Combustion Systems Dynamics Laboratory (CSDL) at Virginia Tech, which has a background of experimental work in combustion dynamics [98, 99], laminar and turbulent combustion [100], multiphase flow [101] and optical diagnostics [102]. The combustor is schematically shown in Figure 3.1, and it was designed for evaluating flame holder concepts for afterburner applications and for developing and demonstrating advanced laser diagnostic techniques.

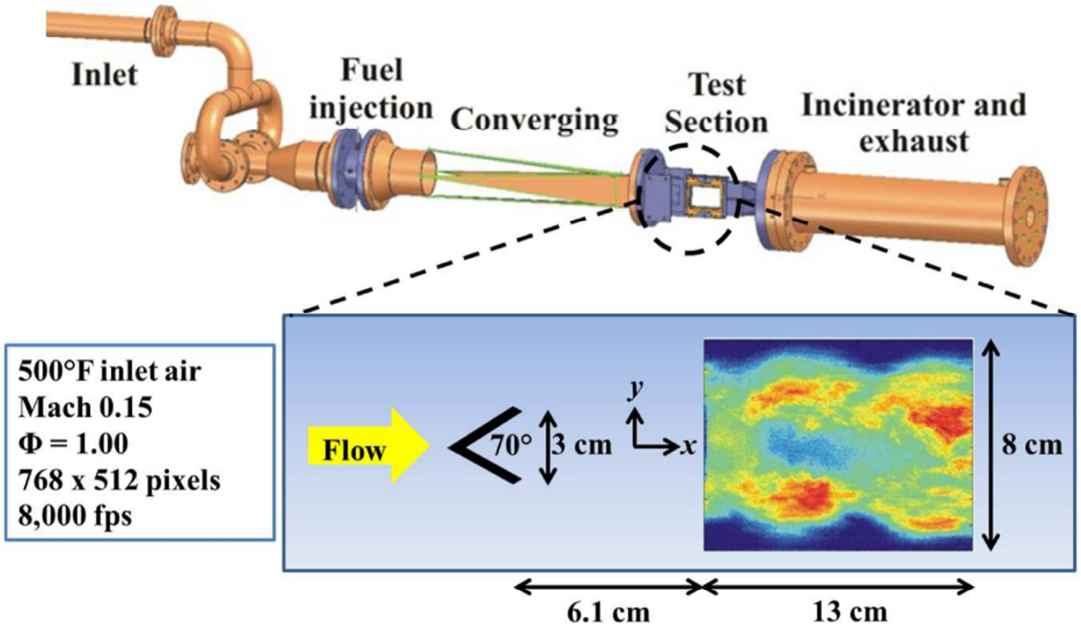

Figure 3.1. Illustration of the experimental setup and a typical chemiluminescence imaging measurement.

A Kaeser FS440 air compressor supplies air to the test facility at a flow rate up to 0.7 kg/s (1.5 lbm/s) and pressure up to 10 atm (150 psia). An electrical heater can preheat the air (unvitiated) up to 650 K (700 F) before it enters the inlet of the test rig. After heat transfer and compressibility effects are included, the envelope of possible inlet temperatures and bulk flow Mach numbers is shown in Figure 3.2 [23]. Fuel injection occurs downstream of the inlet, but sufficiently far upstream of the flameholder so that the fuel and air are fully mixed when they reach the flameholder and are burned.

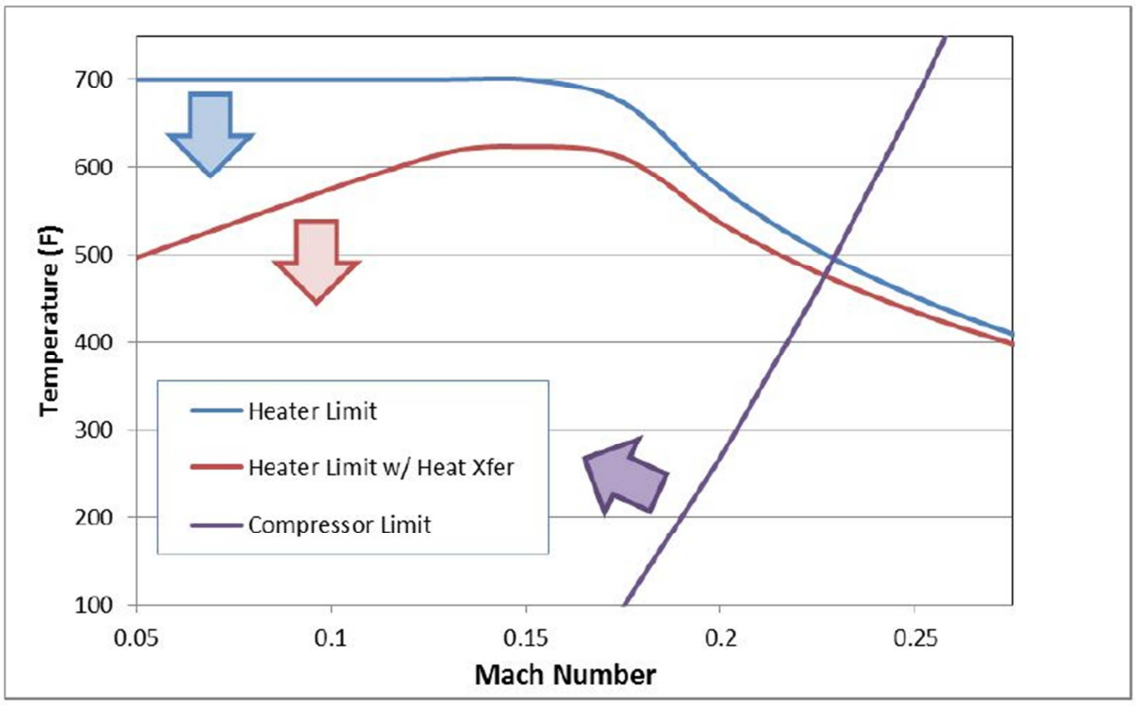

Figure 3.2. Augmentor test section and Mach number limitations from facility constraints [23]

A cross sectional schematic of the modular augmentor rig is shown in Figure 3.3. The fuel used in this study was kerosene. The fuel injection section has a circular cross section with a diameter of 20 cm. A converging section (140 cm in length) then transitions the flow into the rectangular cross-section at the facility's test-section. A

choke plate is installed immediately upstream of the injection section to isolate the experiment acoustically from the rest of the air supply.

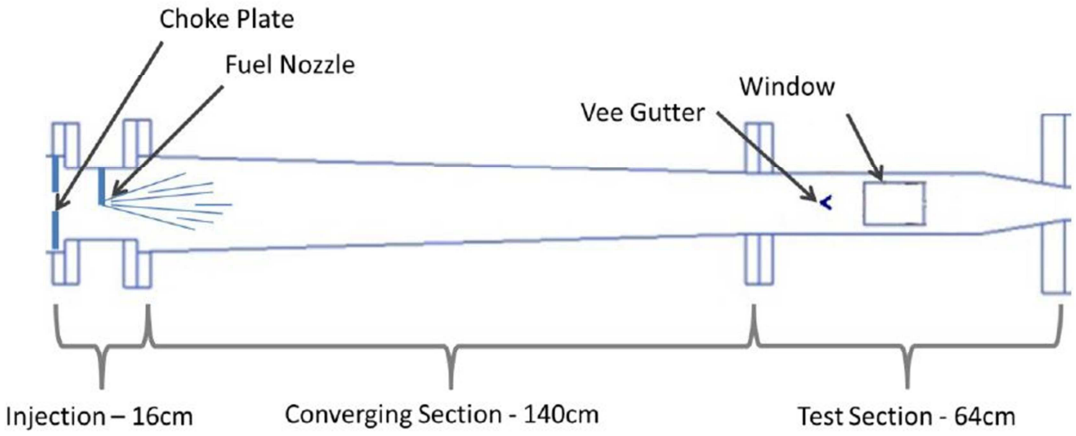

Figure 3.3. Augmentor development rig cross-sectional schematic [103]

The rectangular test-section has a length of 20.3 cm (*x* direction), height of 11.4 cm (*y* direction), and depth of 5.1 cm (*z* direction). The test section is equipped with three windows, a pair of side windows that are 13 cm (length) × 9 cm (height), and a single top window that is 2.5 cm (width) × 13 cm (length). The measurements used in this study were taken from one of the side windows, with an example chemiluminescence image and the corresponding conditions also shown in Figure 3.1. Specifics of the geometry of the test section and the optical windows are provided in the inset of Figure 3.1 or via the CAD model in Figure 3.4. To mitigate the risk of overheating and window fouling, the windows are film-cooled. The windows are also designed as bolt-on modules that can be removed between tests for cleaning, to minimize maintenance downtime due to window fouling issues. The test section is designed to accommodate the testing of various flame holder designs; however, this work was conducted with a vee-gutter flame holder with its

geometry and dimensions shown in Figure 3.1. After the test section, the combustion gas enters an incinerator section before exhausting.

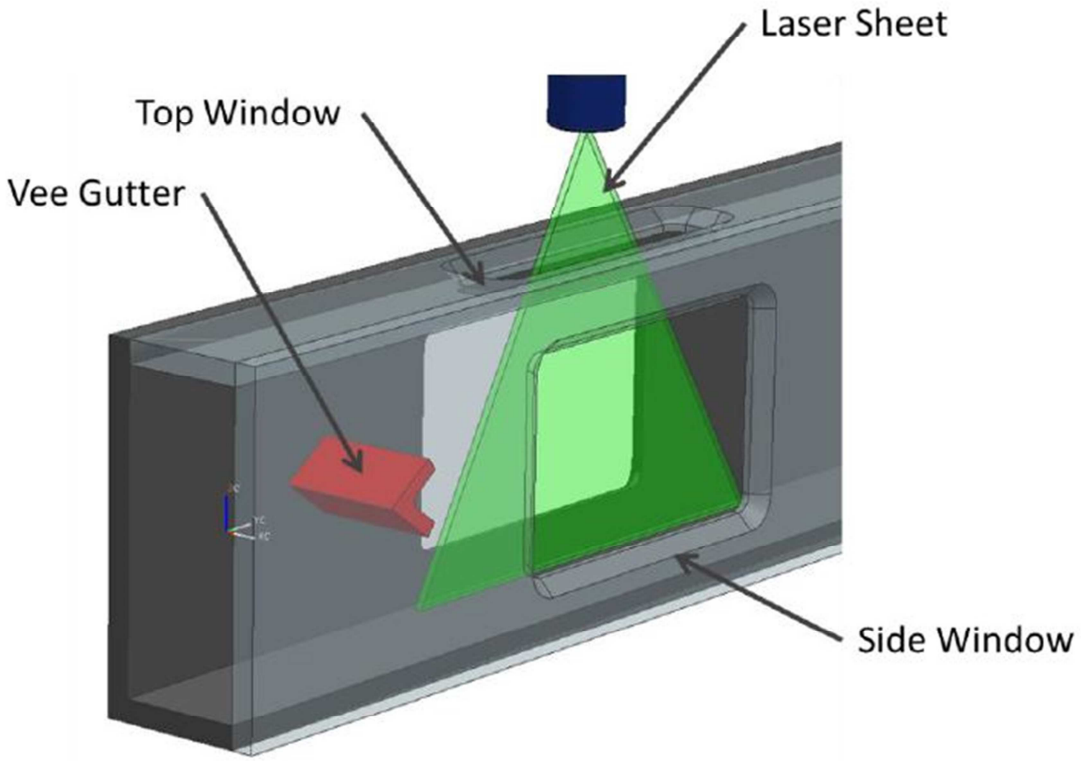

Figure 3.4. Transparent view of CAD model of the vee-gutter test section [23]

Chemiluminescence measurements were performed during the tests. The chemiluminescence data were captured using a Photron SA4 camera equipped with a Sodern lens (100f/2.8 CERCO 2178), capable of imaging in the UV range of 250 to 410 nm with an intensifier. The camera uses a monochrome CMOS detector that provides a frame rate of 3,600 frames per second (fps) with 1,024×1,024 resolution, and up to 500,000 fps at reduced resolutions. In this current work, chemiluminescence measurements were collected for durations of 0.5 second or longer. Unfiltered measurements were imaged at 8,000 fps with a resolution of 768 x 512 pixels, yielding a

spatial resolution of 0.17 mm/pixel. A sample unfiltered measurement and its corresponding test conditions are shown in the inset of Figure 3.1

Filtered chemiluminescence of CH^* near 430 nm was imaged with a narrow band filter (Andover Co.) centered at 430 nm with a FWHM of 10 nm. These measurements were performed at 5,000 fps with a resolution of 1,024 × 800 pixels, yielding a spatial resolution of 0.13 mm/pixel. Our results in this work have shown that both unfiltered and filtered measurements yielded virtually the same characteristic frequencies in all measurements; however, the CH* data will only be shown in the post-processed results.

Tests were performed within a range of experimental conditions in terms of equivalence ratio (from 0.7 to 1.0), inlet air temperature (from 533 to 588 K), and Mach number (from 0.1 to 0.2). Measurements were acquired both under stable combustion conditions and under transient blow off conditions. The specific test conditions that will be compared for this vee-gutter work are shown in the test matrix below.

Table 3.1. Vee-gutter CH* chemiluminescence testing conditions

Test	**Equivalence Ratio, ϕ**	**Bulk Mach number**	**Inlet Temperature, F**	**Condition**	**Camera Rate, Hz**	**# of Frames**
1	1.0	0.15	500	Stable	5,000	6,985
2	1.0	0.20	500	Stable	5,000	6,985
3	1.0-0.7	0.15	500	Unstable	5,000	3,315

3.2. Stable Combustion

Stable combustion was achieved through the following process. The augmentor development rig was preheated to a prescribed 500 °F by flowing continuous preheated air through the test section until thermal equilibrium was reached. This was determined via internal probe and external surface mounted K-type thermocouples. Fuel was then added and an electrical spark was discharged to ignite the fuel and air mixture. The combustion reaction was sustained for a prolonged period of time (approximately 10+ minutes) until thermal equilibrium was once again attained. Once this condition was reached, the exact testing parameters of equivalence ratio and air mass flow rate were set remotely. After the condition was locked into the computer, the diagnostics were initiated. This procedure was repeated for test conditions 1 and 2 and is labeled as "stable" combustion throughout the rest of this dissertation.

3.2.1 Fourier Analysis

As a comparable starting point for analyzing the chemiluminescence results for the vee-gutter, a Fourier transformation was conducted on the images, similar to Steinberg et al. [80]. The Fourier analysis transforms the signal measured in the time domain into the frequency domain, thusly revealing the characteristic frequencies. For the type of 2D (two-dimensional) imaging measurements shown in Figure 3.1, either a multidimensional Fourier transform can be performed, or the dimensionality of the measurements can be reduced first for a subsequent 1D Fourier analysis. For instance, the centroid of the chemiluminescence measurements can be extracted to describe the overall spatial fluctuation of the flame, and a 1D Fourier analysis can then be applied to the

centroid data, as illustrated by the results for test 1, shown in Figure 3.5. Panel (a) of Figure 3.5 shows the *x* and *y* spatial fluctuation of the centroid obtained from set 1 of chemiluminescence images measured on a stable flame. The relatively small fluctuation in the *y* centroid illustrates the overall symmetry of the flame relative to the mid-plane of the vee-gutter (under stable combustion). Panel (b) shows the power spectrum of the *x* and *y* centroid obtained by applying Welch's method [104] to the Fourier transformed results, revealing a peak frequency of 478 Hz or Strouhal number of 0.20 in the *x* direction fluctuation and no distinct frequency component in the *y* direction.

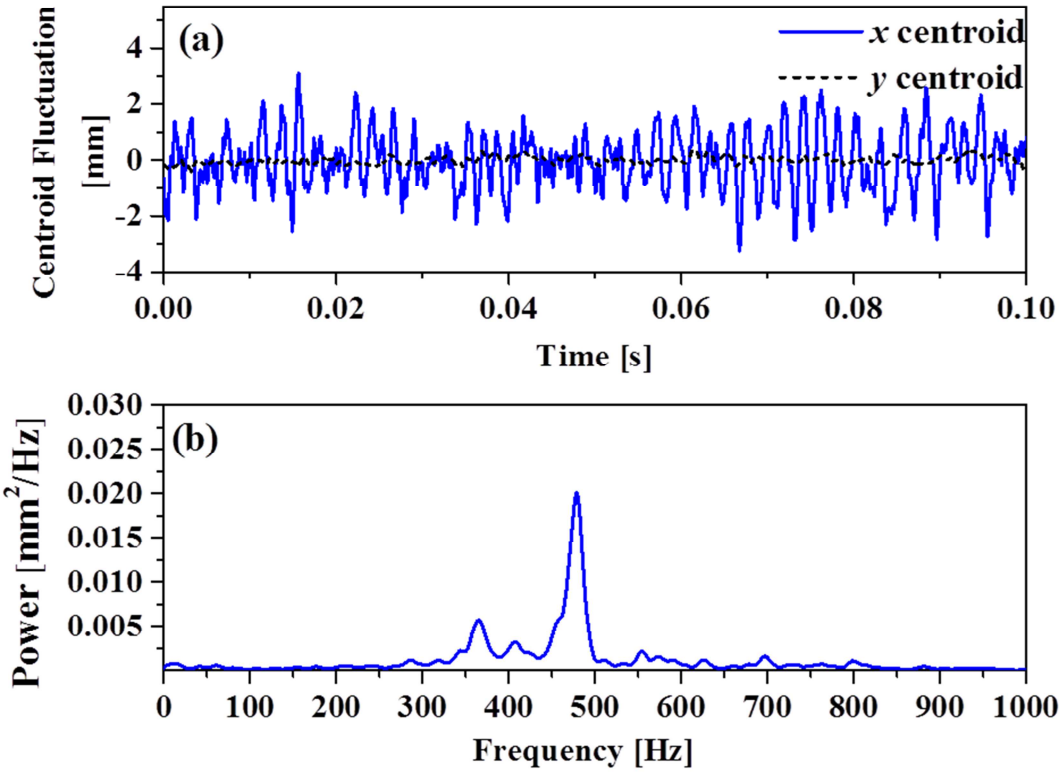

Figure 3.5. Panel (a) x and y direction centroid of chemiluminescence images measured at test condition 1. Panel (b): the power spectrum of the x and y direction centroid obtained by Fourier transformation.

The same analysis was conducted on the test results from condition 2. The power spectrum of the *x* and *y* centroid obtained by Fourier transformation in shown in Figure 3.6.

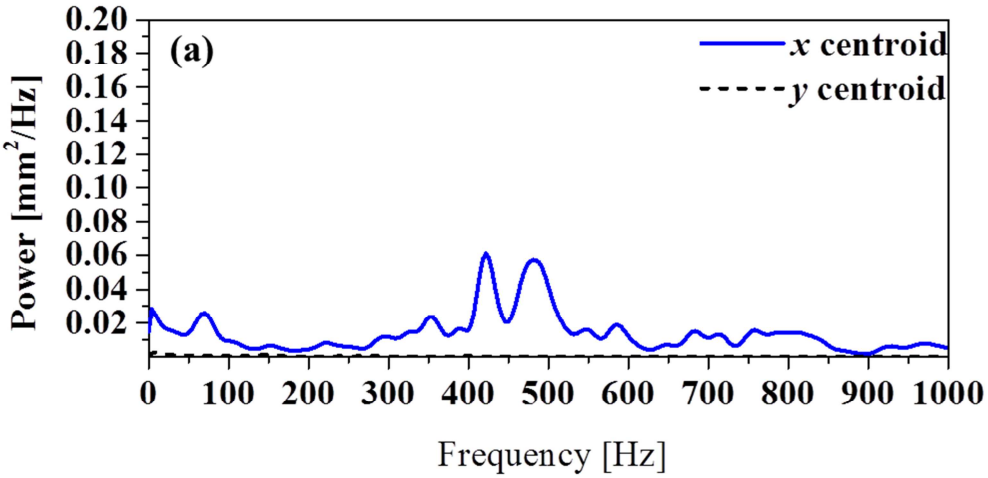

Figure 3.6. Test condition 2 power spectrum of the x and y direction centroid obtained by Fourier transformation

When comparing the results from Figure 3.5 (b) and Figure 3.6, two distinct differences are observed. First, the magnitudes of all characteristic frequencies in Figure 3.6 have been significantly reduced, by 33% to be exact. This phenomenon occurs due to the decreased residence time in the symmetric flamelets, thus limiting the interaction between the turbulent flame shedding structures and the flow shear layer. This limited interaction allows the reaction to proceed more smoothly, which is shown by the decreased magnitudes in the frequency domain of the power spectra. Second, symmetric characteristic frequency peaks are observed in the *x* centroid in Figure 3.6, that correspond to 422 Hz and 490 Hz or Strouhal numbers of 0.14 and 0.16, respectively. This is different than the single characteristic frequency peak observed at 478 Hz in Figure 3.5.

3.2.2. Proper orthogonal decomposition analysis

To extract the large coherent structures of heat release, proper orthogonal decomposition was applied to each stable test condition. The vee-gutter shedding structure exhibited very pronounced coherent structures with the first four eigenmodes containing 98% of the total energy in the system. These four eigenmodes are shown in Figure 3.7 and Figure 3.8 for test conditions 1 and 2, respectively.

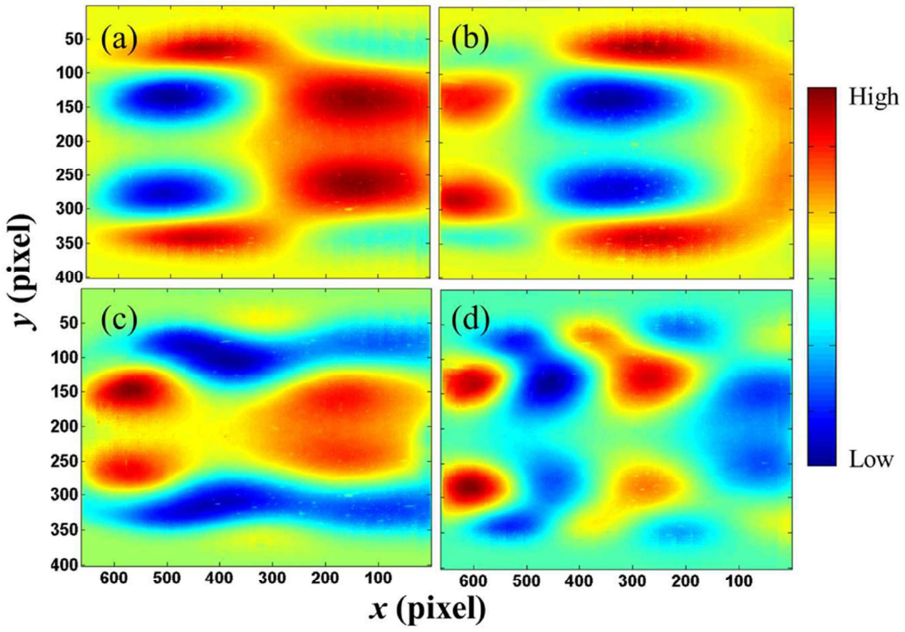

Figure 3.7. The first four eigenmodes of flame structure obtained from POD based on chemiluminescence measurements of test condition 1.

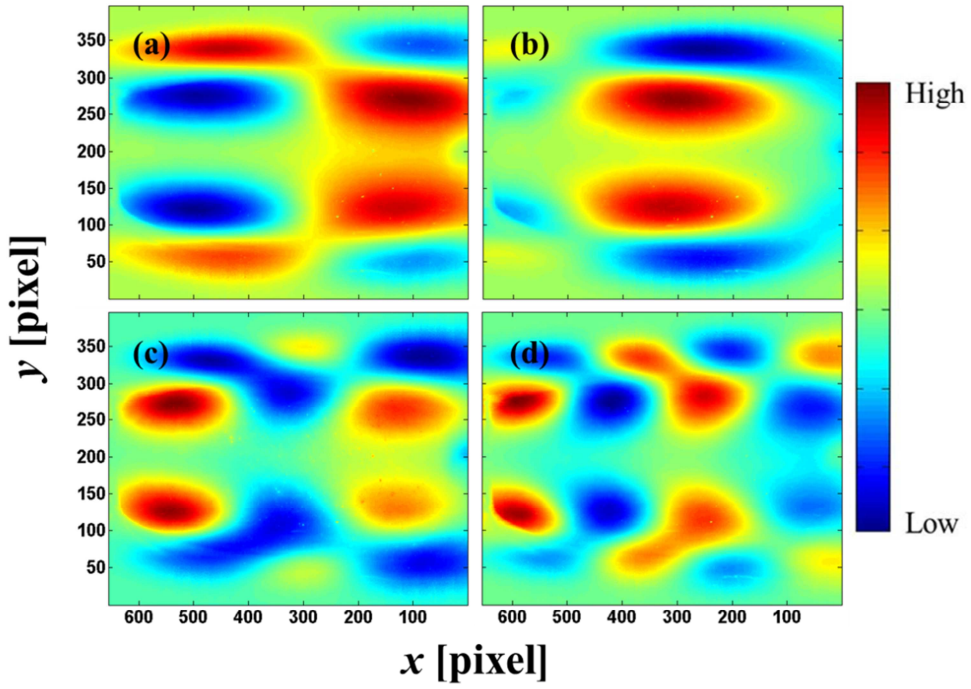

Figure 3.8. The first four eigenmodes of flame structure obtained from POD based on chemiluminescence measurements of test condition 2.

The dominant structures appear similar between both conditions, but upon closer examination the dominant structures in eigenmode 1, Panel (a) of Figure 3.7 are greater in area and much closer to the centerline of the image, where they are interacting with each other. This interaction contributes to producing the periodic, symmetric, shedding pattern that literature shows so prevalently with vee-gutter wakes. For test condition 2, shown in Panel (a) of Figure 3.8, the coherent structures are slightly farther apart, smaller in area when compared to the test condition 1 in Figure 3.7 and don't appear to interact as much, producing a much smoother burning reaction. This smoother burner was also observed visually in individual instantaneous snapshots shown in Figure 3.9 as well in the numerical LES reconstruction outlined in Blanchard et al. [22] and shown in Figure 3.10.

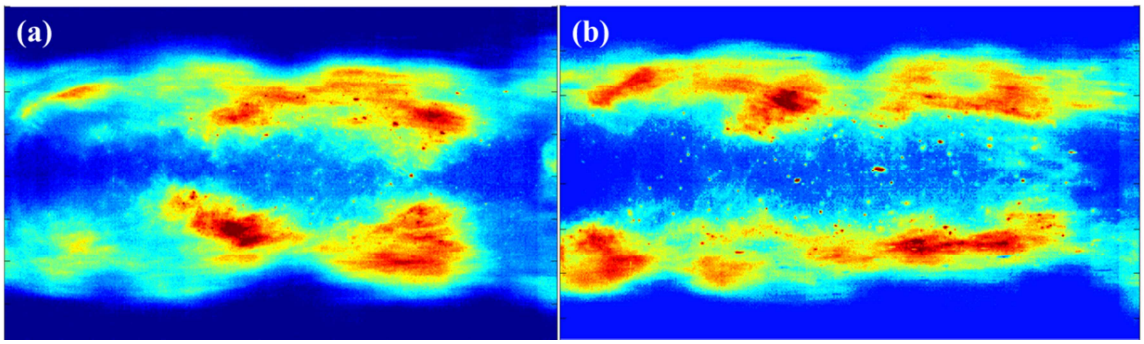

Figure 3.9. Panel (a): Instantaneous Mach 0.15 chemiluminescence image. Panel (b): Instantaneous Mach 0.20 chemiluminescence image.

This reduction in characteristic frequency for increasing Mach number inlets is further shown by transforming the dominant temporal coefficients with a Fourier transform. Panel (a) of Figure 3.11 shows the first two temporal coefficients a_1 and a_2 obtained from the POD analysis, and Panel (b) shows the power spectrum obtained by performing a Fourier analysis on a_1 and a_2. As the results show, both power spectra are similar and exhibit the same peak frequency of 478 Hz, which agrees with that obtained from Figure 3.5 and is similar to other results [80].

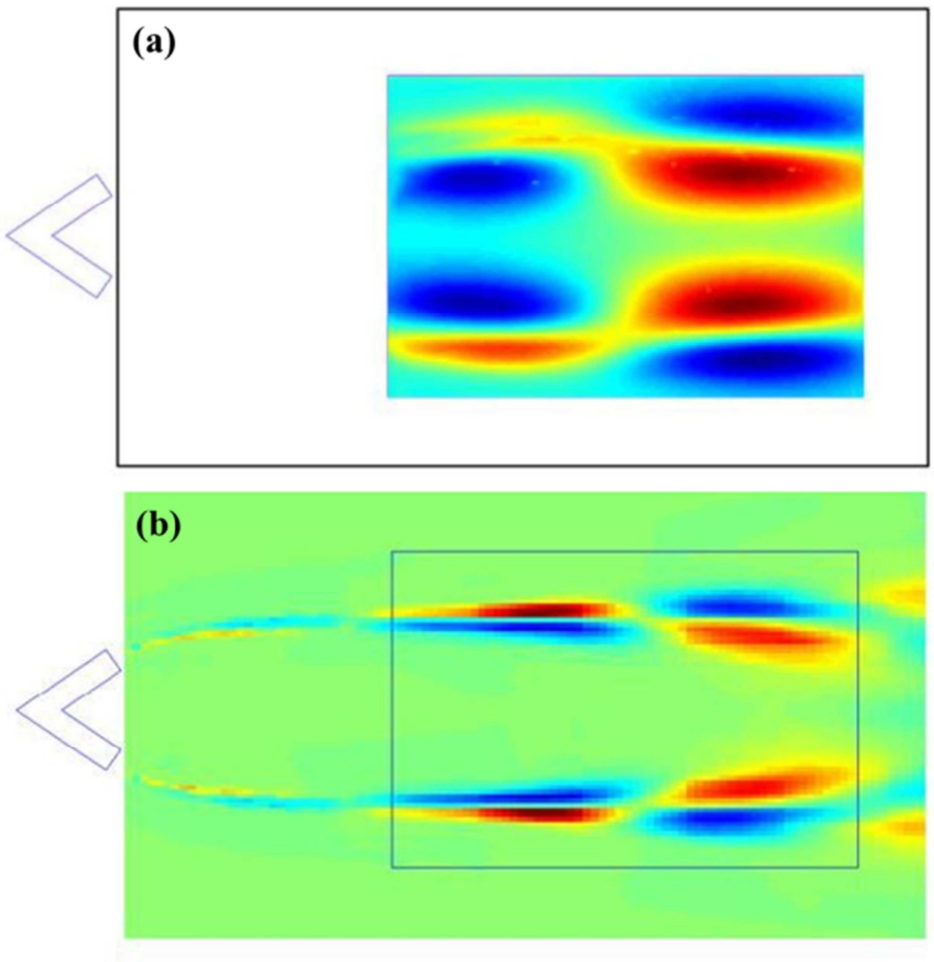

Figure 3.10. Panel (a) Eigenmode 1 of Mach 0.20 chemiluminescence. Panel (b): Projection of integral of heat release in the LES model [22]

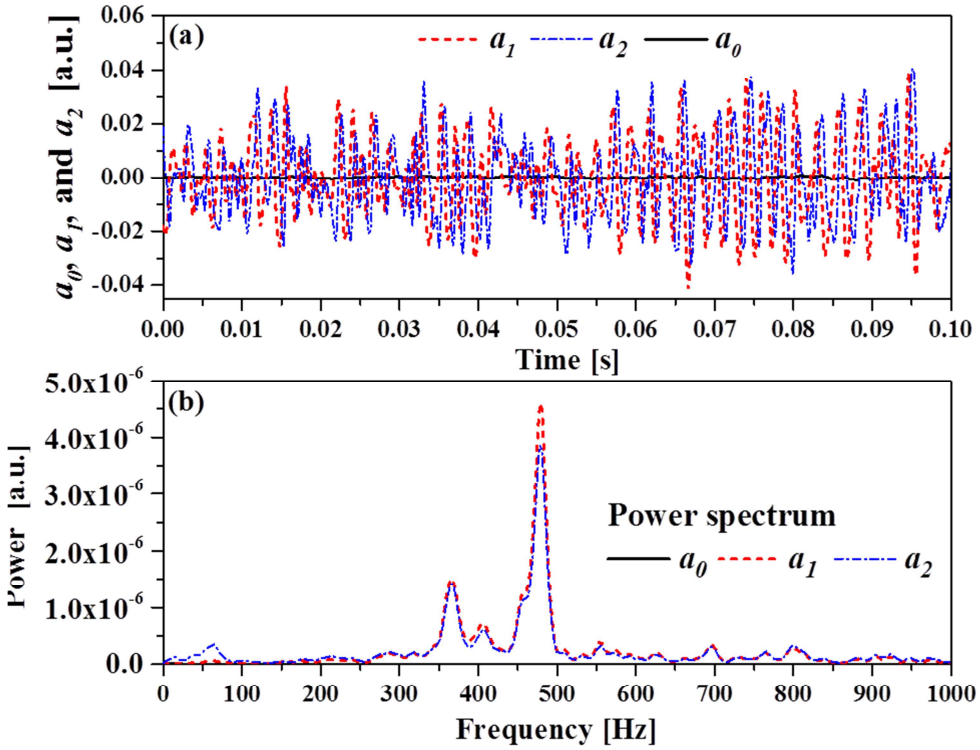

Figure 3.11. Panel (a): the magnitude fluctuation of chemiluminescence eigenmode temporal coefficients 0-2, based on the measurements from test 1. Panel (b): the power spectrum of Fourier transform of eigenmode temporal coefficients for test 1

Note that the data obtained from the 0th eigenmode is also included in Figure 3.11 for comparative purposes. Panel (a) evidently shows the lack of fluctuation in a_0 for such a stable flame, due to fact that the 0th eigenmode simply represents the average of all the measurements in the series, which is numerical subtracted from each individual image to normalize the fluctuation. Panel (b) confirms the observation made from Panel (a) by showing that 1) the power spectrum corresponding to a_0 is several orders weaker in magnitude than those obtained from the first two eigenmodes, and 2) the lack of a distinct frequency component in the power spectrum corresponding to a_0.

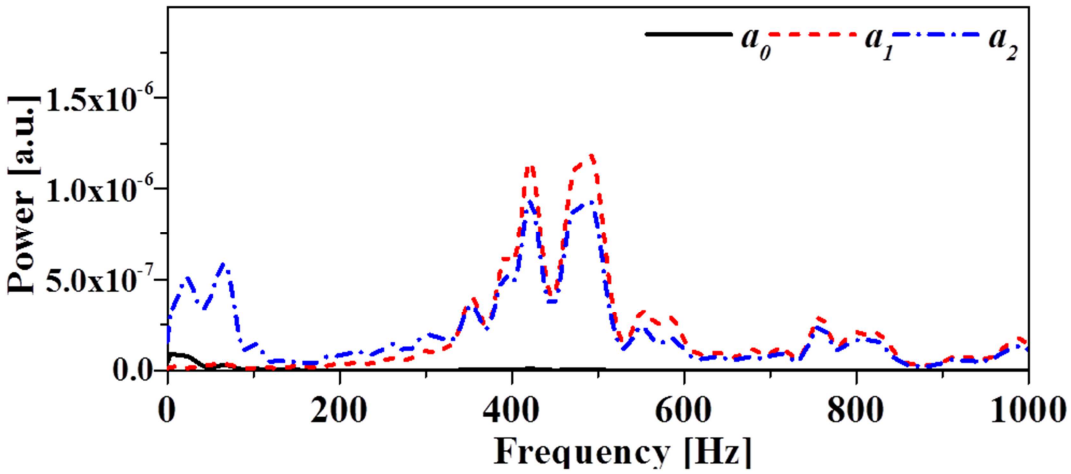

Figure 3.12. The power spectrum of Fourier transform of eigenmode temporal coefficients for test 2

The power spectrum for test condition 2, shown in Figure 3.12, reveals the same two conclusions as with the Fourier method in Chapter 3.2.2 when compared to Figure 3.11. The frequency doublet is evident at the same frequencies of 422 Hz and 490 Hz as shown in Figure 3.6, and the magnitudes are almost an order of magnitude smaller than shown in Figure 3.11.

3.2.3. Continuous wavelet transform analysis

To take the analysis a step further the temporal coefficients were processed with a continuous wavelet transform to visualize the time-frequency relationship with these two stable conditions. This analysis was completed because, as mentioned above in Section 2.5 in Chapter 2, both the Fourier and POD transforms have their limitations when applied to nonlinear and unsteady (sometimes even chaotic) phenomena of interest in combustion research. The WA method overcomes these restrictions by the careful choice of the wavelet basis. The results from test condition 1 are shown in Figure 3.13.

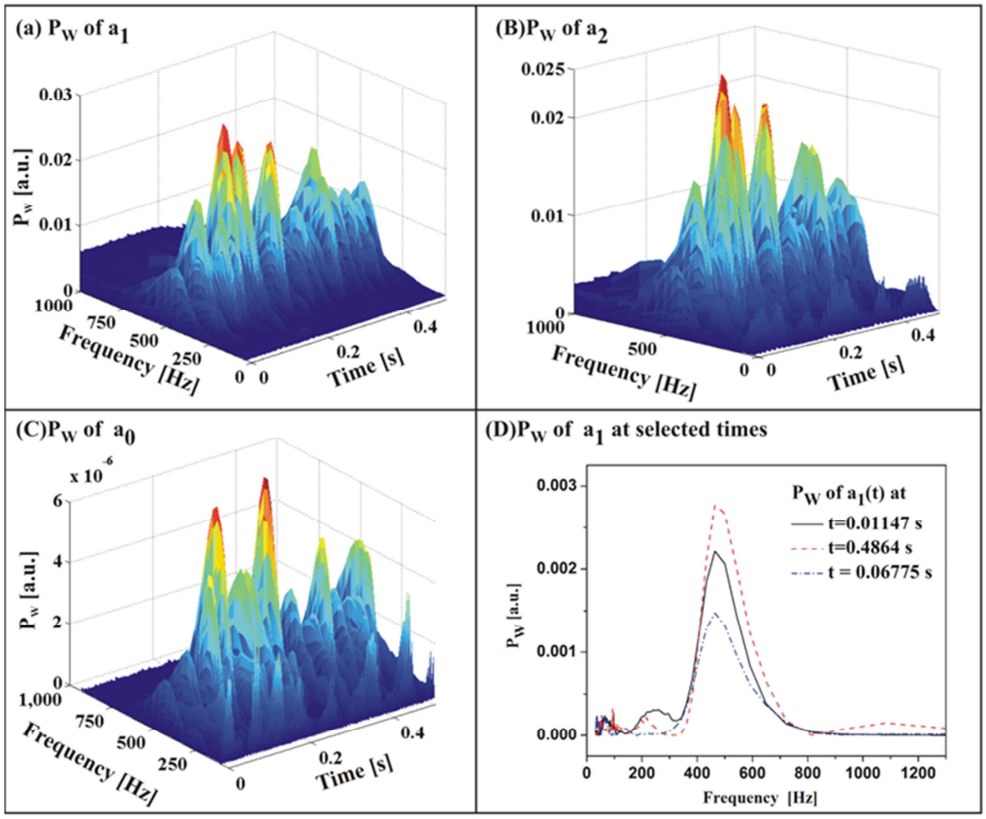

Figure 3.13. Panel (a)-(c): spectrograms of $a_1(t)$, $a_2(t)$ and $a_0(t)$, respectively. Panel (d): spectrogram of $a_1(t)$ at three selected times.

Panels (a), (b), and (c) show the spectrograms; and Panel (d) examines the spectrogram of $a_1(t)$ at a few selected times. Several observations can be made by comparing the wavelet spectrogram in Figure 3.13 to the Fourier power spectrum shown in Figure 3.11. First, the wavelet spectrogram reveals the same dominant frequency component in $a_1(t)$ and $a_2(t)$ as the Fourier power spectrum (near 478 Hz), as observed from results in Panel (a), (b), and (d). Second, the wavelet spectrogram in Panel (c) also reveals the lack of a dominant frequency component in $a_0(t)$, for the same reason discussed in Section 3.2.1 with the Fourier method. Third, all results in Figure 3.13 show that the dominant frequency component (or the lack of it) is relatively stable in time,

because the data used here are obtained under stable combustion. However, the wavelet spectrograms do reveal certain degrees of temporal variations of the magnitude of the energy contained at each time step, which is consistent with the chaotic nature of the high-speed combustion process. These temporal variations will become more pronounced for unsteady combustion processes, described in further detail in Chapter 3.3, providing insights unattainable from the Fourier analysis.

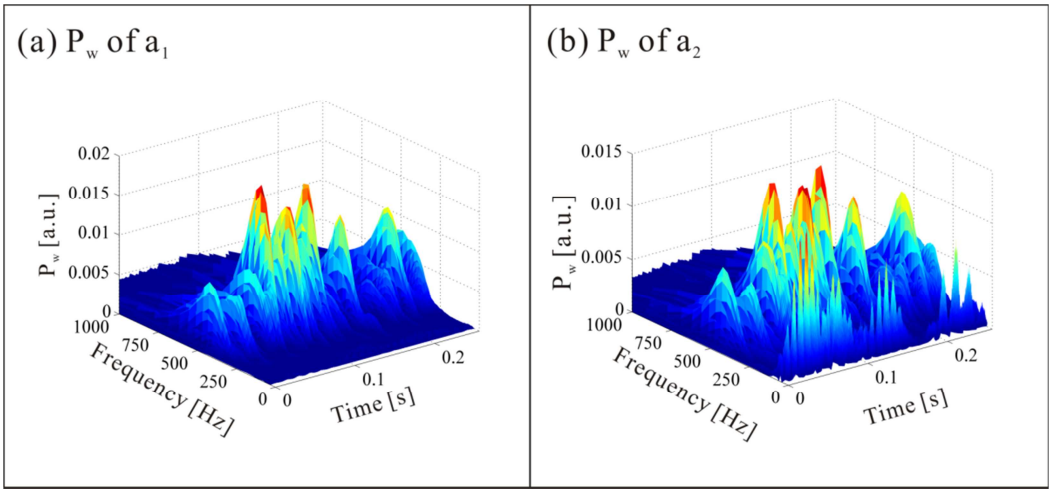

Figure 3.14. Panel (a)-(b): spectrograms of $a_1(t)$ and $a_2(t)$, respectively.

The same analysis was completed on the results from test condition 2. The results from applying the CWT to the dominant temporal coefficients are shown in Figure 3.14. Note that the temporal coefficient associated with the mean, $a_0(t)$, is not shown for the reasons described earlier. Two major conclusions can be drawn from Figure 3.14. First, the magnitudes from test condition 2 show the same reduced trend when compared to their test condition 1 counterparts, as was also shown with the Fourier and POD analysis. However, the second conclusion deviates from the previous analyses because the frequency doublet, observed from the Fourier and POD analyses can now be seen to oscillate as a function of time, as seen in panels (a) and (b) of Figure 3.14

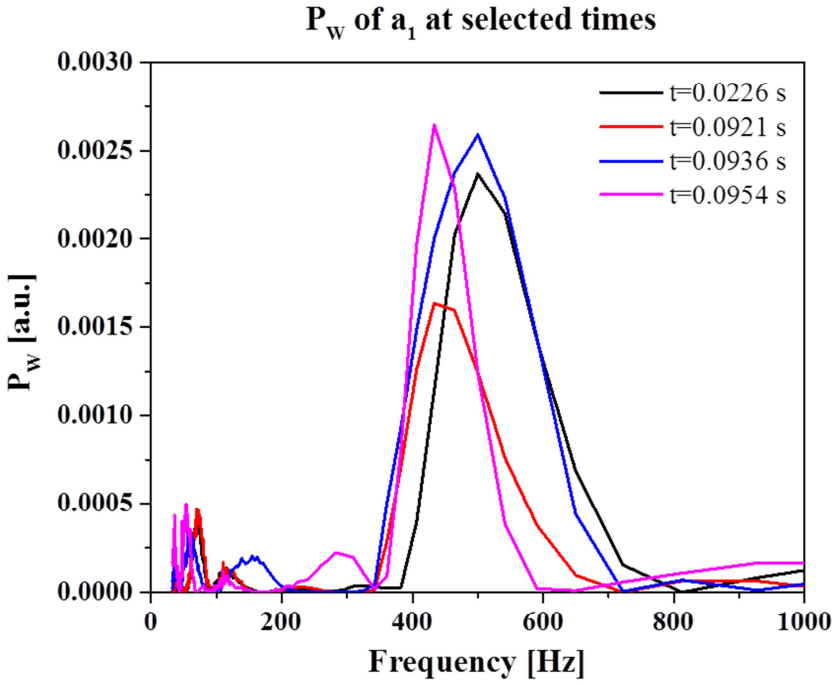

Figure 3.15. Spectrogram of $a_1(t)$ temporal coefficient at four selected times.

However, this is better viewed when looking at the individual wavelets at different time steps, as observed in Figure 3.15. The dominant frequencies observed with the CWT, shown in Figure 3.15, are 433 Hz and 500 Hz, or Strouhal numbers of 0.14 and 0.16, respectively, which are similar to the previous frequencies, but not identical.

3.3. Unstable Combustion

Flame blow off is an important issue in practical power and propulsion systems. It is a highly transient process that can lead to global consequences. However, current understanding of blow off under practical conditions is incomplete and many important aspects of blow off dynamics remain at a phenomenological stage [21]. To study the blow off process, this work used the experimental setup shown in Figure 3.1 to create

lean blow off (LBO) processes by decreasing the fuel/air equivalence ratio according to the scheme displayed in Figure 3.16.

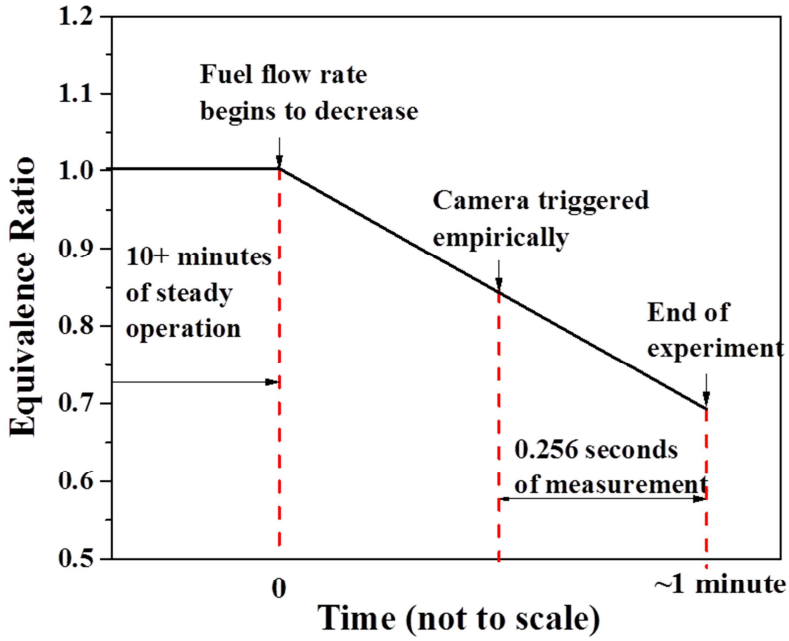

Figure 3.16. Illustration of the measurement sequence in the Lean Blow Out (LBO) experiment.

The experiment consisted of four steps. First, a stable flame with unity equivalence ratio was maintained under the desired Mach number and inlet temperature for more than 10 minutes to reach thermal equilibrium and establish steady state operation, as discussed in Chapter 3.2. Second, the fuel flow rate was decreased linearly. As shown in Figure 3.16 the moment when the fuel flow rate began to decrease was defined as time zero. Third, the camera was empirically triggered to start capturing chemiluminescence images after the fuel/air equivalence ratio was reduced to a certain level. In our experiments, we observed that a chugging sound preceded the LBO processes, which was used as an

empirical indicator to trigger the camera. Fourth, the experiments were terminated either when the camera ran out of memory of when the flame was completely extinguished. With this current scheme, the duration between time zero and the end of the experiments typically lasted 1 minute. Therefore, an ideal experimental setup would require the capability to capture high speed chemiluminescence images for about 1 minute, starting at time zero and lasting until the flame completely extinguishes. Due to the inability to predict the LBO processes and the imaging capabilities that we had in this work, we had to depend on multiple trials to obtain a satisfactory set of data and we could only capture a fraction of the LBO processes.

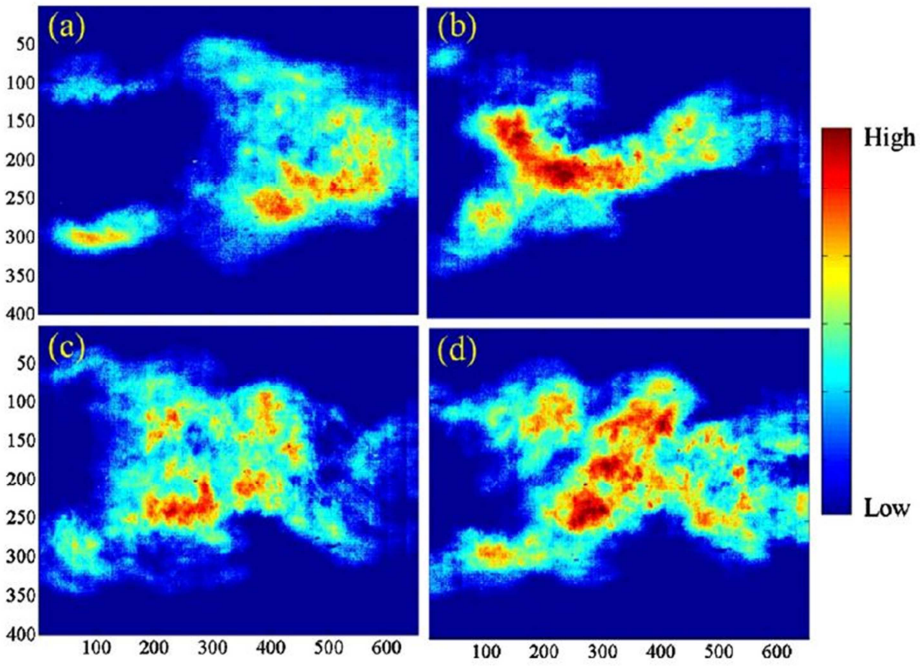

Figure 3.17. Instantaneous chemiluminescence images at the times selected in Panel (c) of Figure 3.15.

For instance, the results to be shown in the rest of this section were obtained based on a set of chemiluminescence measurement captured during 0.256 seconds, as illustrated in

Figure 3.16. For this particular set of data, the inlet temperature was 533 K, the nominal Mach was 0.15, and the flame was completely extinguished at an equivalence ratio of 0.7. Due to the transient nature of the LBO process, this data set will be referred to as unstable combustion for the remainder of the dissertation. Figure 3.17 corroborates this transient claim by showing the instantaneous chemiluminescence images measured at the four selected times depicted in Figure 3.15. For comparison, Figure 3.1, shows an instantaneous chemiluminescence image captured under stable combustion consistent with test condition 1. Under such unstable conditions, it is only natural for the combustion to possess different power spectrum structures at different times, which is shown in the upcoming Section 3.3.3.

3.3.1 Fourier Analysis

The same intensity-weighted centroid Fourier analysis outlined in Section 3.2.1 was completed for the results of the LBO case. Figure 3.18 shows the spatial fluctuation in millimeters and upon comparison to the stable combustion case [Figure 3.5 (a)], the main differences are evident. First, the mean fluctuation in the *x* direction is on the order of 10 mm compared to 2 mm with the stable combustion cases. This larger fluctuation is indicative of the lower frequency, larger oscillation observed in the reaction zone observed with unstable combustion. Second, there are small scale (~1-2 mm) fluctuations in the *y* direction, where previously there was no fluctuation. This fluctuation indicates a small deviation from the symmetric shedding pattern observed during stable combustion.

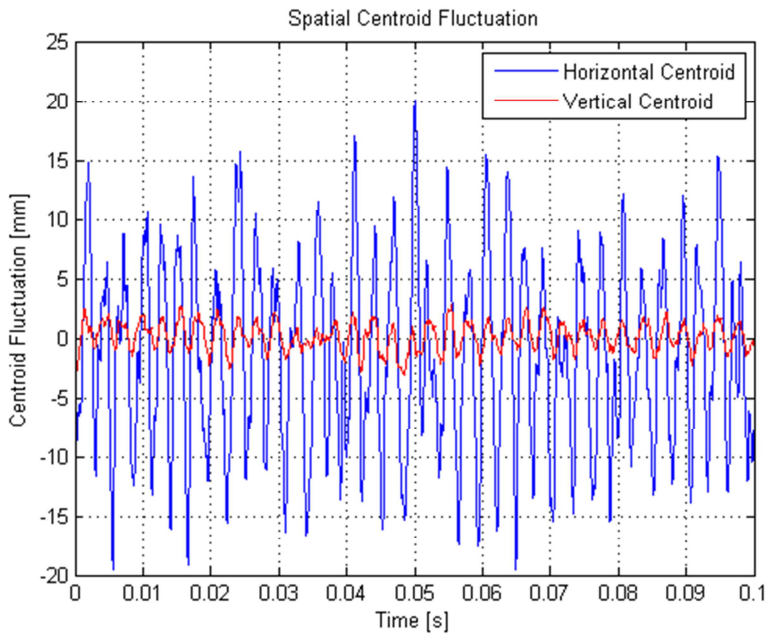

Figure 3.18. Intensity weighted centroid spatial fluctuation during test condition 3

Figure 3.19 shows the results obtained by performing a Fourier analysis on the *x* and *y* centroids of the chemiluminescence data as described in Chapter 3.2.1. Two observations can be made on the results obtained by the Fourier transform shown here. First, the result suggests a single frequency peak near 348 Hz. However, due to the transient nature of the LBO process, the interpretation of such a frequency peak is less straightforward compared to those observed in the stable combustion processes, as the dominant frequency component may vary during the process. Secondly, there exists a larger, lower frequency component, which is expected for LBO combustion due to its large amplitude, low frequency components observed in literature [105]

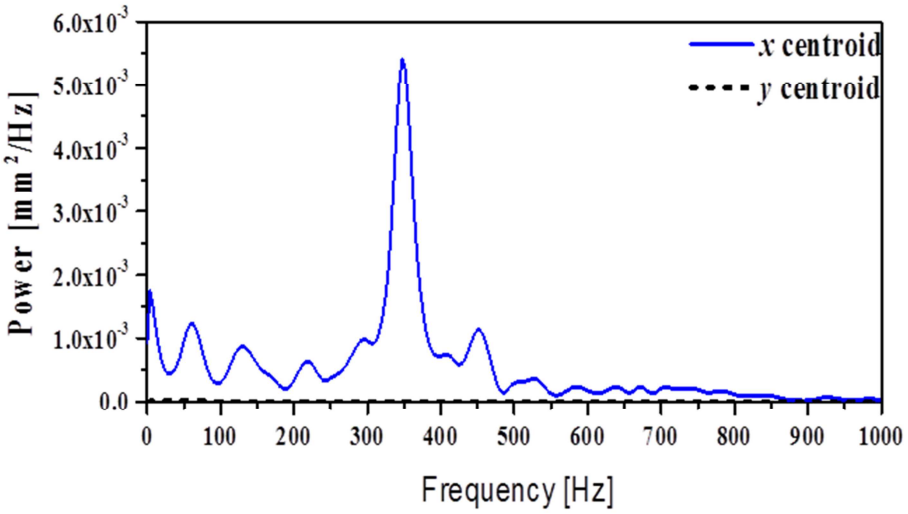

Figure 3.19. Power spectrum obtained by performing a Fourier transform on the intensity-weighted centroids during the LBO experiment.

3.3.2. Proper orthogonal decomposition analysis

Figure 3.20 shows the results obtained by performing a Fourier analysis on dominant POD coefficients as described in Chapter 3.2.2. The same two observations can be made on these results as those obtained by the Fourier transform shown in Figure 3.19. First, the result suggests a single frequency peak near 348 Hz. However, due to the transient nature of the LBO process, the interpretation of such a frequency peak is less straightforward compared to those observed in the stable combustion processes, as the dominant frequency component may vary during the process. Secondly, there exists a larger, lower frequency component, than observed with the centroid Fourier analysis. This is because the dominant coherent structures typically exhibit low frequency oscillatory motion; therefore, if only those dominant modes are examined, we should expect to see larger, low frequency amplitudes in the POD spectrum.

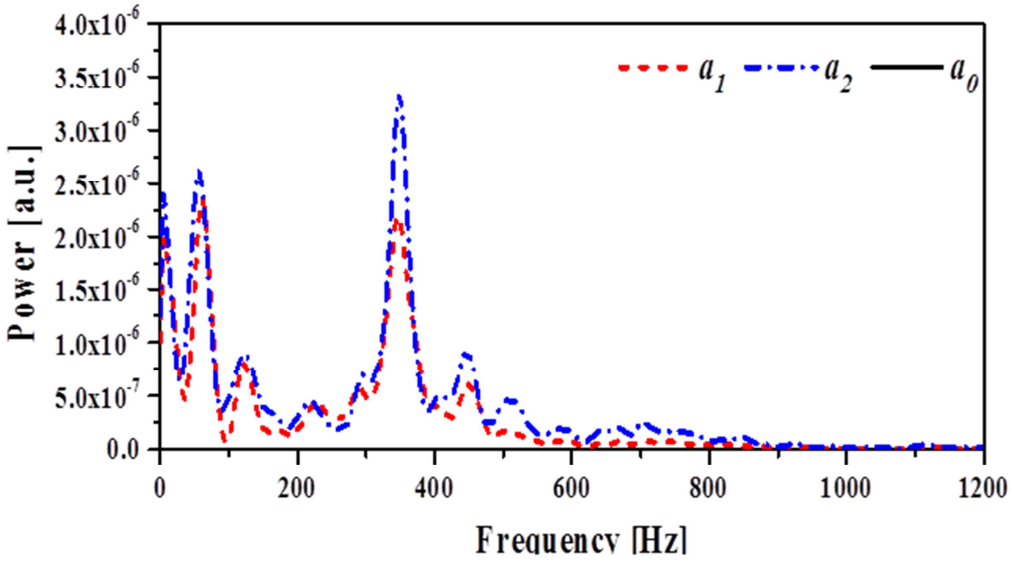

Figure 3.20. Power spectrum of $a_1(t), a_2(t)$ and $a_0(t)$ POD temporal coefficients

3.3.3. Continuous wavelet transform analysis

Lastly, Panel (a) of Figure 3.21 shows the spectrogram obtained by performing the CWT on the *x* centroid of the LBO chemiluminescence measurements, and Panel (b) highlights the spectrogram at the same selected times as in Figure 3.15 and Figure 3.17. Comparison between the results in Figure 3.21 and Figure 3.22 show that the spectrograms obtained from both the temporal coefficients and the centroid data 1) agree quantitatively in terms of the overall structure and the unsteadiness of the frequency components, and 2) agree qualitatively in terms of the location of the peak frequency as can be seen by comparing the results in Panel (c) of Figure 3.22 to those in Panel (b) of Figure 3.21. These results further confirm the insensitivity of the CWT when applied to different target signals extracted from the raw measurements, as already observed in Chapter 3.2 when the CWT was applied to analyze stable combustion processes.

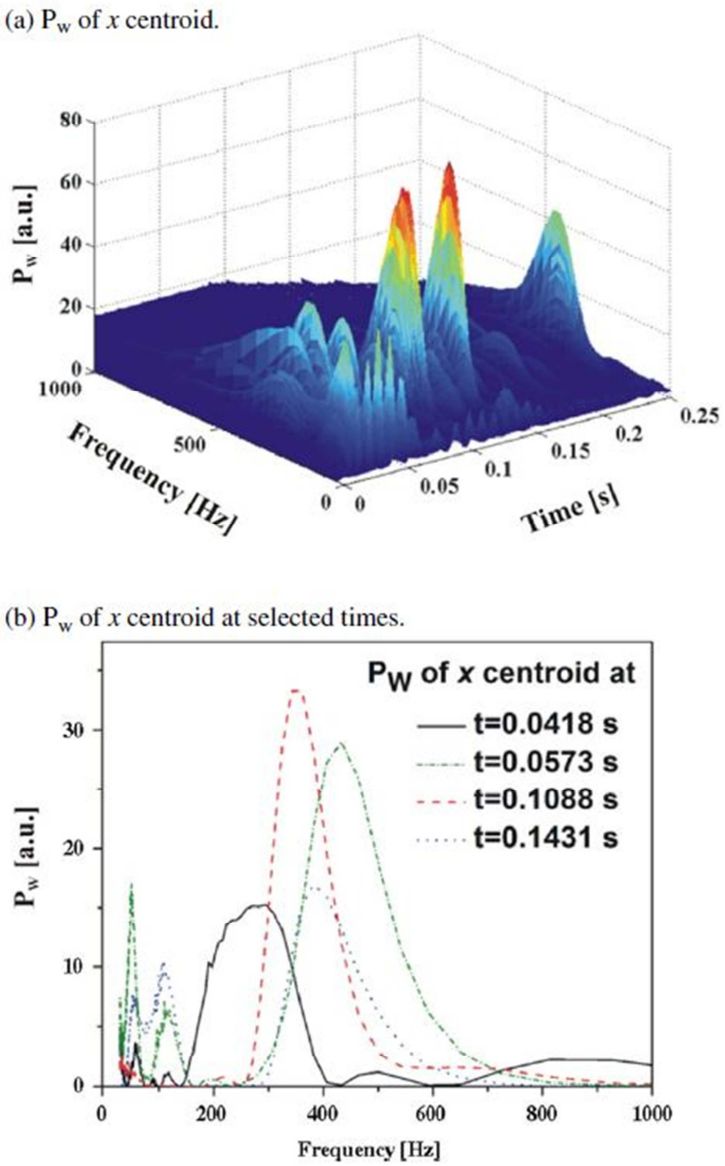

Figure 3.21. Panel (a): spectrogram obtained by performing a CWT on the x *centroid of the LBO data. Panel (b): spectrUSeogram of* x *centroid at four selected times.*

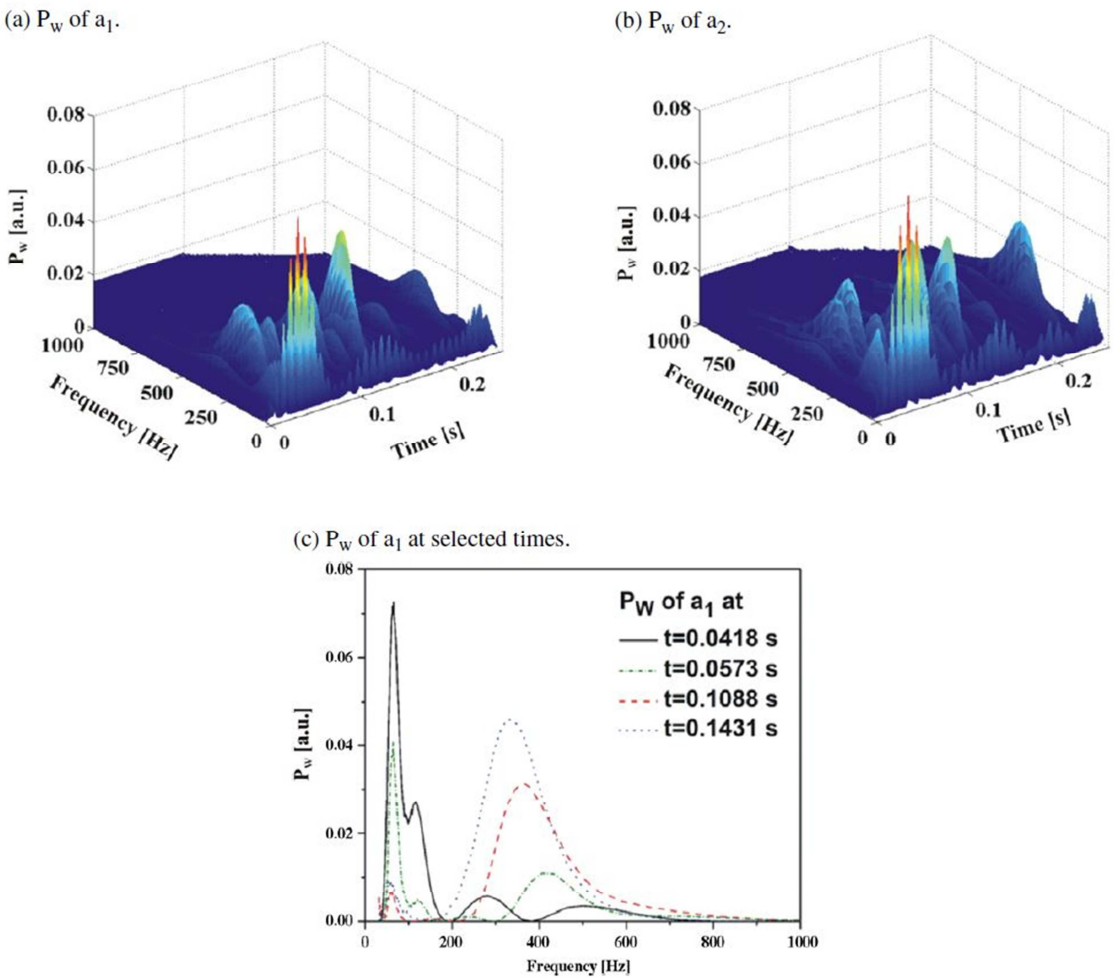

Figure 3.22. Panel (a) and (b): Spectrogram by performing the CWT on $a_1(t)$ and $a_2(t)$ of the LBO data. Panel (c): spectrogram of $a_1(t)$ at four selected times.

3.4. Summary

Three major conclusions can be drawn from the results obtained in this work. First, under stable combustion conditions, power spectra obtained from all three methods are similar both quantitatively and qualitatively, in terms of the overall shape of the power spectra and the location of the peak frequency. Second, under unstable and transient combustion conditions, the CWT method is capable of revealing the dynamics

of the frequency components in the measurements, while traditional Fourier and PCA methods encounter application restrictions. Third, our results support the suitability and usefulness of the CWT method in analyzing practical transient signals. The CWT method is applicable to discrete signals, insensitive to the choice of wavelet basis, and insensitive to the target signal extracted from the raw measurements. These features were demonstrated in the analysis of the LBO processes using the CWT method, overcoming the restrictions of traditional Fourier and PCA methods. Extension of the CWT method for the analysis of other types of measurements (such as PIV and planar laser induced fluorescence) is straightforward. These results and observations are expected to be useful for the quantitative analysis of high-speed flow and combustion measurements. Particularly, the CWT's ability to analyze nonstationary and practical signal makes it attractive for revealing flow-flame interactions during unstable and transient combustion processes.

Chapter 4. Measurements and analysis of supersonic combustion flows

4.1. Experimental operating conditions

The supersonic combustion measurements were performed in the supersonic wind tunnel housed in Research Cell 19 at Wright-Patterson Air Force Base. The facility is capable of operating continuously with peak stagnation conditions of 2,860 kPa and 922 K at flow rates up to 15.4 kg/s [30, 106]. For the current experiments, a generic cavity-based flameholder configuration was used as shown in Figure 4.1. The entire flow path is 15.2 cm wide, and there are two ports in the base of the cavity located 1.9 cm on either side of the symmetry plane to accommodate spark plugs [30]. The two spark plugs were fired simultaneously (approximately 100 mJ/pulse) during the experiments and served as the sole source to ignite the mixture within the cavity. Fuel (C_2H_4) was injected into the cavity from eleven holes in the cavity closeout ramp. A flow Mach number of 2, corresponding to a flight value of $M_{flight} \approx 4$, total temperature of approximately 610 K and total pressure of approximately 483 kPa was used for all experiments. There was optical access from both the side and top through quartz windows, allowing through multiple views examination of the cavity ignition and burning process. While the entire cavity could be viewed through the side windows, the top window restricted the view to the central 10 cm of the 15.2 cm wide flow path.

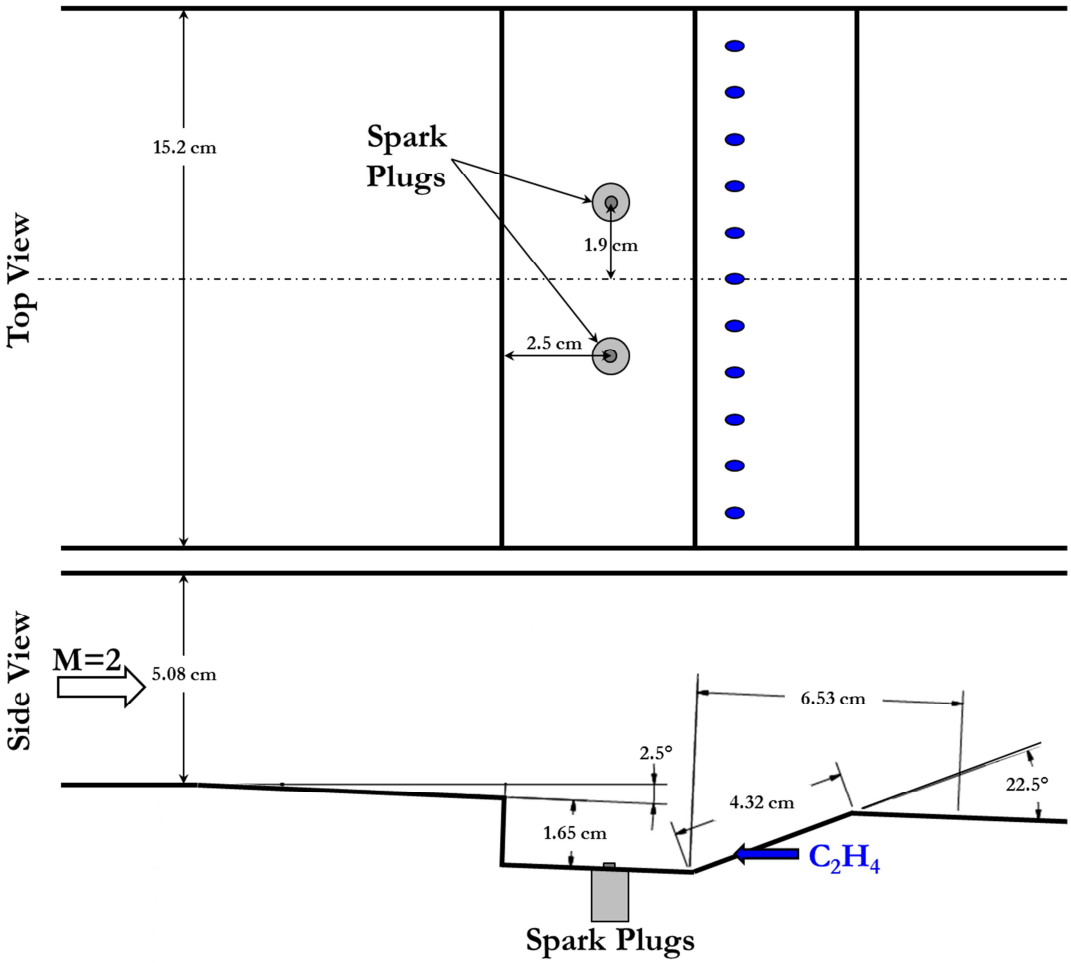

Figure 4.1. Schematic of cavity based flowpath.

Extensive measurements have been performed on this supersonic tunnel previously. For example, previous supersonic PIV measurements were completed in Research Cell 19's scramjet rig by Tuttle et al. [41] focusing on both reacting and non-reacting conditions. Of the four reacting tests completed, one was for a fuel-lean condition of 56 standard liters per minute (SLPM) of ethylene, whereas another was for a fuel-rich condition of 99 SLPM. It was the intention of this work to repeat these same conditions with more diagnostics to compare current data with previous data. Various datasets were

captured with both PIV and chemiluminescence imaging, and the two sets processed in this work for chemiluminescence are listed in Table 4.1.

It is worth mentioning that measuring chemiluminescence in practical systems has been a major challenge [107-109]. This challenge is further exacerbated when making multidimensional measurements because they typically require multiple viewing angles and locations in an already space limited system [110-112]. A solution to this issue has been investigated in recent years with the use of fiber-based endoscopes (FBEs) [113-115]. FBEs have a relatively small footprint (~10 mm fiber core) when compared to a standard high-speed camera and they are flexible enough to install in any limited, optical access environment. Due to these benefits and the need for multiple perspectives to map the flame structure, FBEs were used in this work to record emission from seven different viewing projections.

When using FBEs, there are several critical issues that have to be resolved in order to successfully capture images. Including, measuring the exact viewing registration of each FBE and evaluating the degradation of spatial resolution, signal uniformity and signal linearity of each projection during transmission. Viewing registration is simply the process of determining the precise position and orientation of each FBE in physical space in order to transform from a three-dimensional world coordinate system to a two-dimensional image system. This work adopted an open source MATLAB tool developed specifically for this purpose, to determine the exact location of each FBE in world coordinates [116]. To account for the spatial resolution or how sharply features in an image can be resolved, a known calibration target was used. Optical fibers have been known to attenuate signals and distort images based on fiber length and position;

therefore, care had to be taken to use proper lens systems and precise alignment procedures to minimize these losses. With these practices in place, sub-millimeter spatial resolution was possible and had also been shown using the same FBE setup as demonstrated in the work by Kang et.al. [113]. For more information on the use of FBEs in 3D combustion measurements, see Kang et al. [113].

As shown in Table 4.1, each chemiluminescence case consisted of 5,000 total frames; however, this included a portion of the set with no combustion, a small ignition event (83 frames) followed by stable combustion. Only the stable combustion portion was analyzed in this work, which consisted of 4,739 frames in total for each case. However, this concept of "stable" combustion proved more difficult to characterize after application of POD to the data set as will be discussed in Chapter 4.3.

Table 4.1. Chemiluminescence Testing Conditions:

Case	1	2
T_0 (F)	636	641
P_0 (psia)	69.9	69.9
Mach	2	2
Fuel Flow Rate (SLPM)	55	95
No. of frames	5,000	5,000
Frame Rate (Hz)	20,000	20,000
Exposure (ms)	0.049	0.049
Total Duration (s)	0.245	0.245

*SLPM refers to standard liters (referenced to 273 K and 1 standard atm) per minute

The experimental setup used for measuring combustion chemiluminescence in this scramjet facility is shown in Figure 4.2

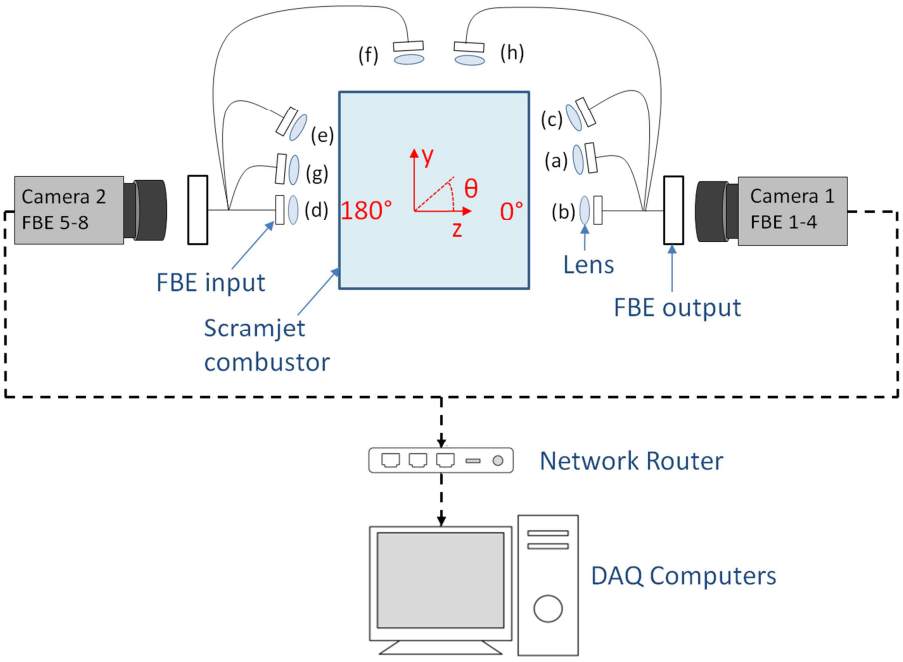

Figure 4.2. Schematic of the experimental setup using 8 FBEs to obtain multi-angle chemiluminescence measurements.

Two high-speed Photron SA-Z cameras were used in combination with 2 FBE bundles. To clearly show the overall setup position relative to the test section, Figure 4.2 shows the layout of the chemiluminescence sensor from the cross-sectional view of the tunnel (i.e., the flow is proceeding into the page). Each FBE bundle consists of one fiber based output and four fiber based inputs as shown. Each camera was precisely synchronized with the other, and the data were transmitted via a network router and recorded on two data acquisition (DAQ) computers in the adjacent control room.

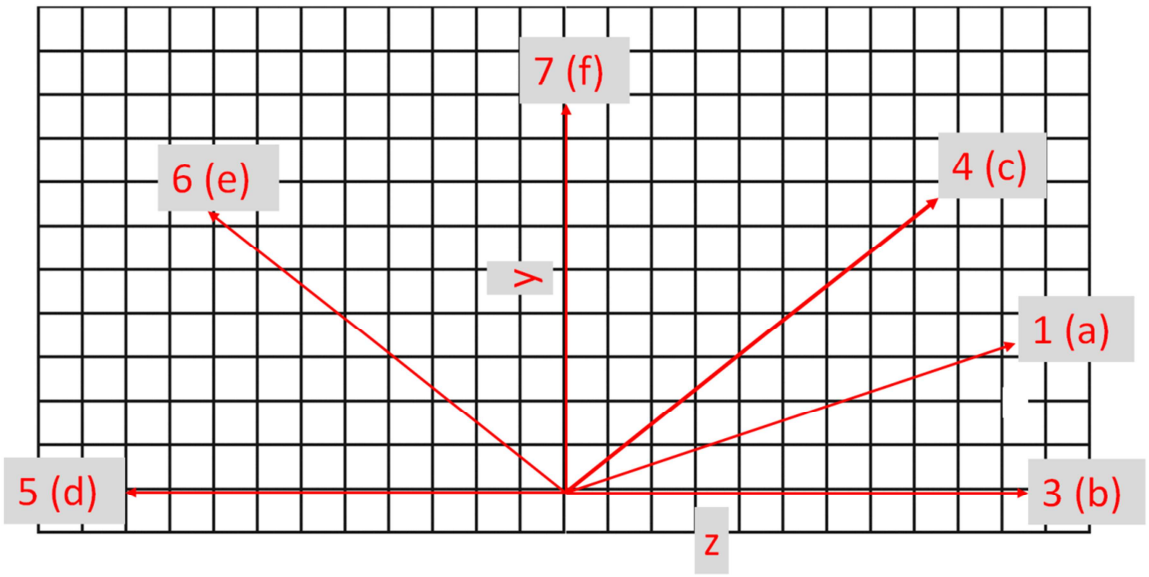

Figure 4.3. Orientations of the 6 FBEs determined from the viewing registration method. The orientations are respectively, (a) FBE1 (17.8 degrees), (b) FBE3 (0.0 degrees), (c) FBE4 (38.4 degrees), (d) FBE5 (180.0 degrees), (e) FBE6 (144.0 degrees), and (f) FBE7 (91.9 degrees).

This work reports results obtained by six FBEs with orientations as shown in Figure 4.3. Using the MATLAB camera calibration toolbox [116] in combination with a calibration target, exact viewing registration angles were calculated. Each FBE was focused onto the same calibration target (from different viewing planes) and from that target, a common focal point was determined. Then each FBE's position and orientation, accounting for spatial degradation, were measured relative to that fixed point in space. The orientations of the FBEs determined using this method are shown in Figure 4.3. These orientations are relative to the horizontal direction (z-axis in Figure 4.2 and the x-axis is defined to be along the direction of the flow in this work), as calculated using the view registration method originally formulated by Bouguet [116] and demonstrated in Kang et al. [117].

An example of the six simultaneous projections, during stable combustion from Case 1, is shown in Figure 4.4. Each image has been oriented such that the flow is proceeding from the left to right. Also, in Panels *(b)*, *(d)*, and *(f)*, lines have been drawn according to the combustor boundaries to help orient the viewer to the precise location of the flame, fuel injection holes and spark plugs. Each image has been artificially colored based on the same intensity scale of each image, where the color red depicts bright (or most intense) regions and blue indicates areas of no signal. This coloring scheme will be adopted for all remaining images in this report.

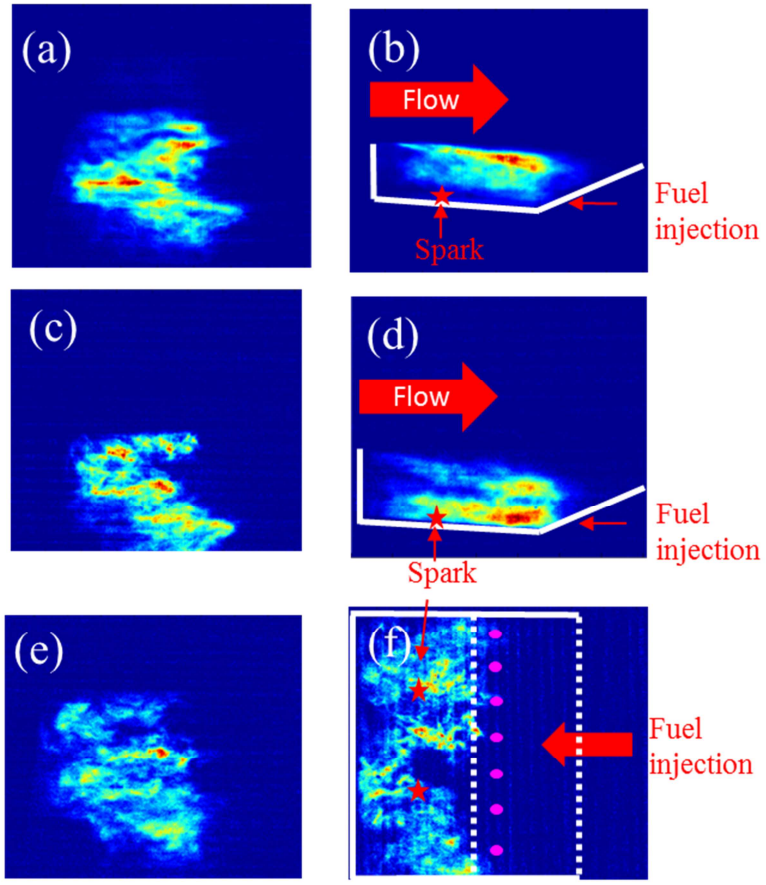

Figure 4.4. A set of instantaneous images obtained by the 6 FBEs simultaneously under the fuel-lean conditions as listed in Table 1.

4.2. Proper orthogonal decomposition analysis

POD analysis was completed on both chemiluminescence cases outlined in Table 4.1 and the results for eigenmodes 1 and 2 are compared in Figure 4.5 through Figure 4.10, respectively. The first major observation from these results is that the POD analysis yielded different mode shapes depending on the view, which is due to the 3D nature of the flame front in the cavity. The benefit of imaging chemiluminescence from different views enables us to analyze each individual view for conclusions about the global chemical reaction.

One such conclusion is depicted in Panel (*b)* of Figure 4.5 and Figure 4.6, which shows the differences in the shear layer flame for the fuel-lean versus the fuel-rich condition, respectively. In the fuel-lean condition there is a singular dominant structure centered in the shear layer, whereas for the fuel-rich case, there are two coherent structures dominating the shear layer and impingement region, respectively. This duality of structures is indicative of non-uniform combustion occurring within the cavity for the fuel-rich case.

Another example of this is the asymmetry observed in the dominant flame structure as a function of position. This is evident upon comparing Panels (*b)* and (*d)* of Figure 4.5 and Figure 4.6. These perspectives correspond to 0 degrees and 180 degrees respectively; therefore, to the casual observed, one would expect the results to be the same, due to the integrated line-of-sight. However, the distinct difference between these panels clearly depicts the non-uniform combustion occurring within the cavity as a function of position. In other words, if a hot spot is located asymmetrically in the cavity, the light scattering solid angle would be larger for one FBE versus the other, thus

resulting in different chemiluminescence structures. This 3D combustion structure is further shown by observing the top view image of each fuel loading case, as shown in Panel (*f)* of Figure 4.5 and Figure 4.6. For Figure 4.5, there exists a larger intensity structure closer to one wall (top wall) than the other. This is hypothesized to be caused from three possible reasons. First, non-uniform heating of the cavity surface would allow for incoming fuel to reach combustible limits sooner at one wall versus the other colder wall. This also creates somewhat of a feedback loop that will continually add heat to the cavity asymmetrically, further sustaining a skewed combustion structured towards one wall or the other. These surface temperatures were not monitored precisely during testing; therefore, this hypothesis cannot be verified at this time. Second, there may exist a more complicated 3D recirculation structure within the cavity that contains more or less vorticity or momentum at differing wall boundaries, which would change the degrees of mixing and/or burning, respectively. This conclusion stems from the asymmetry observed in the coherent structures in Panel (*f)* of Figure 4.6. The coherent structures at the bottom of the figure present as larger in area in comparison to the top structures; indicative of a different flow structure at each wall boundary. Also, a small cold region is just evident in the bottom left corner of the same figure, with a faint, small structure evident at the trailing edge, alluding to a more complicated structure present in the flow. This triangular cold region is not observed at the top, left corner of the same frame, thus implying a combustion reaction occurring within that section. Lastly, this flow effect could be a result of a shock structure at the cavity's leading edge, which asymmetrically affects the flow as it enters the cavity. This could directionally skew the flow entering the cavity towards one wall versus the other, creating the asymmetric, combustion pattern observed

in Panel (*f*) of Figure 4.5 and Figure 4.6. The last two conclusions cannot be validated with the current data set due to the planar nature of the PIV and Schlieren images captured at the centerline of this combustor. This further proves the need for multi-dimensional diagnostics to fully understand complicated combustion flows and benefits of this FBE chemiluminescence experimental setup.

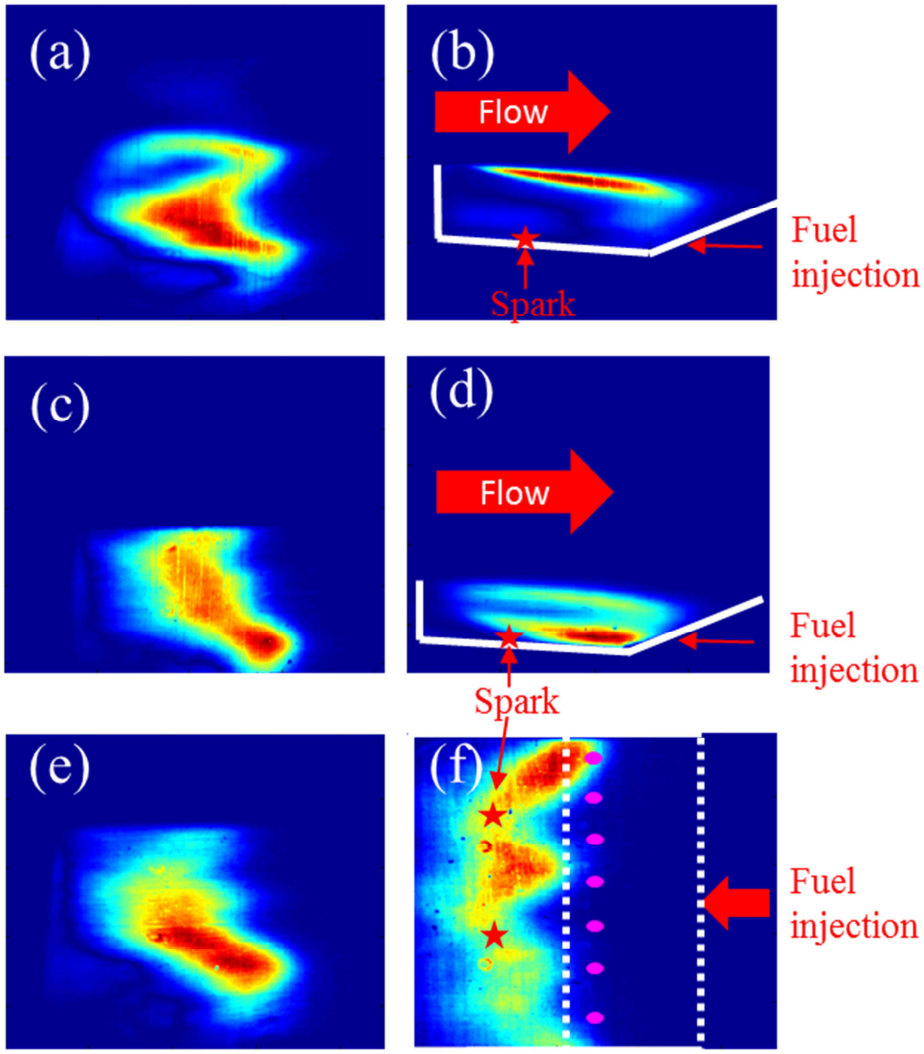

Figure 4.5. First eigenmode of fuel-lean flame.

Other studies, performed with similar conditions and geometry, theorized that a non-uniform combustion occurs due to a fuel-rich lobe that forms on either side of the span

wise centerline, leading to very poor combustion in the upstream end of the cavity coupled with non-uniform burning in the downstream portion of the cavity [30]. This low-temperature fuel-rich region in the upstream cavity section thus inhibits the shear-layer flame from being ignited [30]. The later point is visualized in all panels of Figure 4.5 and Figure 4.6 when comparing the size and shape of the flame structure (red colored region) as well as the relative energy content contained within each eigenmode.

The relative energy percentage of each eigenmode is determined by dividing each corresponding eigenvalue by the sum of all of the eigenvalues in the problem.

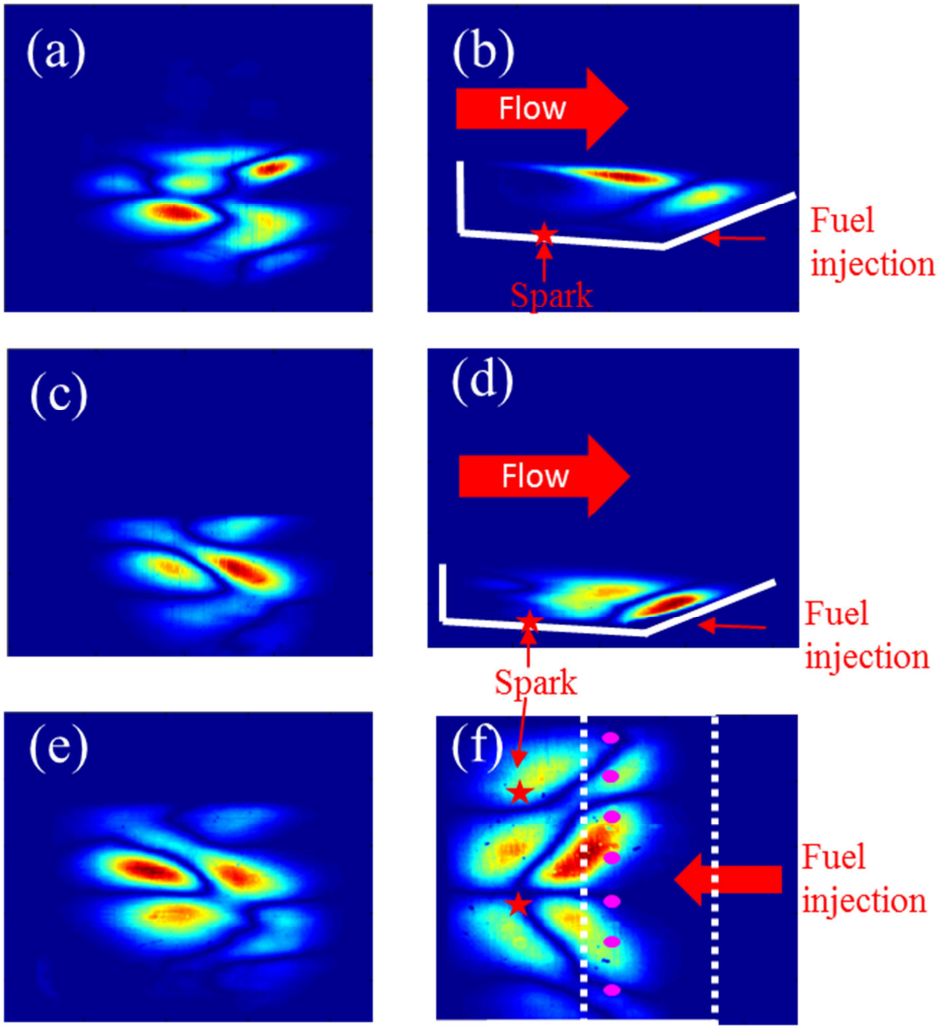

Figure 4.6. First eigenmode of fuel rich flame.

In physical terms, this is a measure of the variance weight of the structure relative to the other structures found by the POD analysis. The relative energy of the fuel-lean case is 44.3%, whereas the fuel-rich case was 16.0%, indicating a more stable variant structure in the fuel-lean condition, as shown in Figure 4.7. Coupled with the low relative energy content was the shorter and wider flame structure in the fuel-rich case.

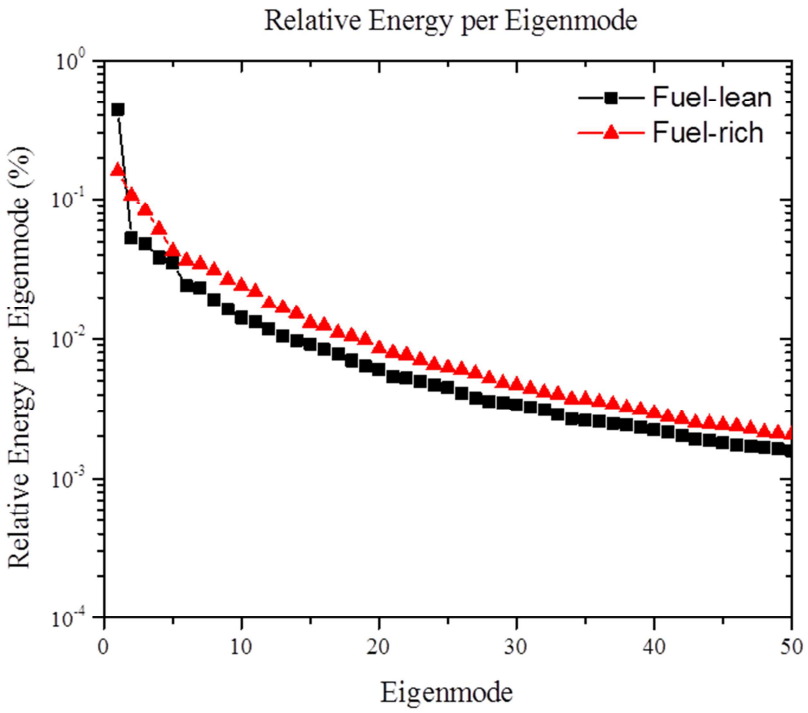

Figure 4.7. Relative energy per eigenmode for fuel-lean and fuel-rich cases.

Upon closer examination of the instantaneous images in this fuel-rich set, the shear layer flame was observed to stabilize prominently in the shear-layer, similar to the fuel-lean case, but then periodically blow out and relight from the impingement section. This is indicative of the dual structures observed in Panel (b) of Figure 4.8.

Another conclusion is the verification that as fuel flow rates increase from low to high fuel loading, the stable combustion region shifts farther downstream in the cavity, similar to Figure 4.9 found in Tuttle et al. [34, 41, 42].

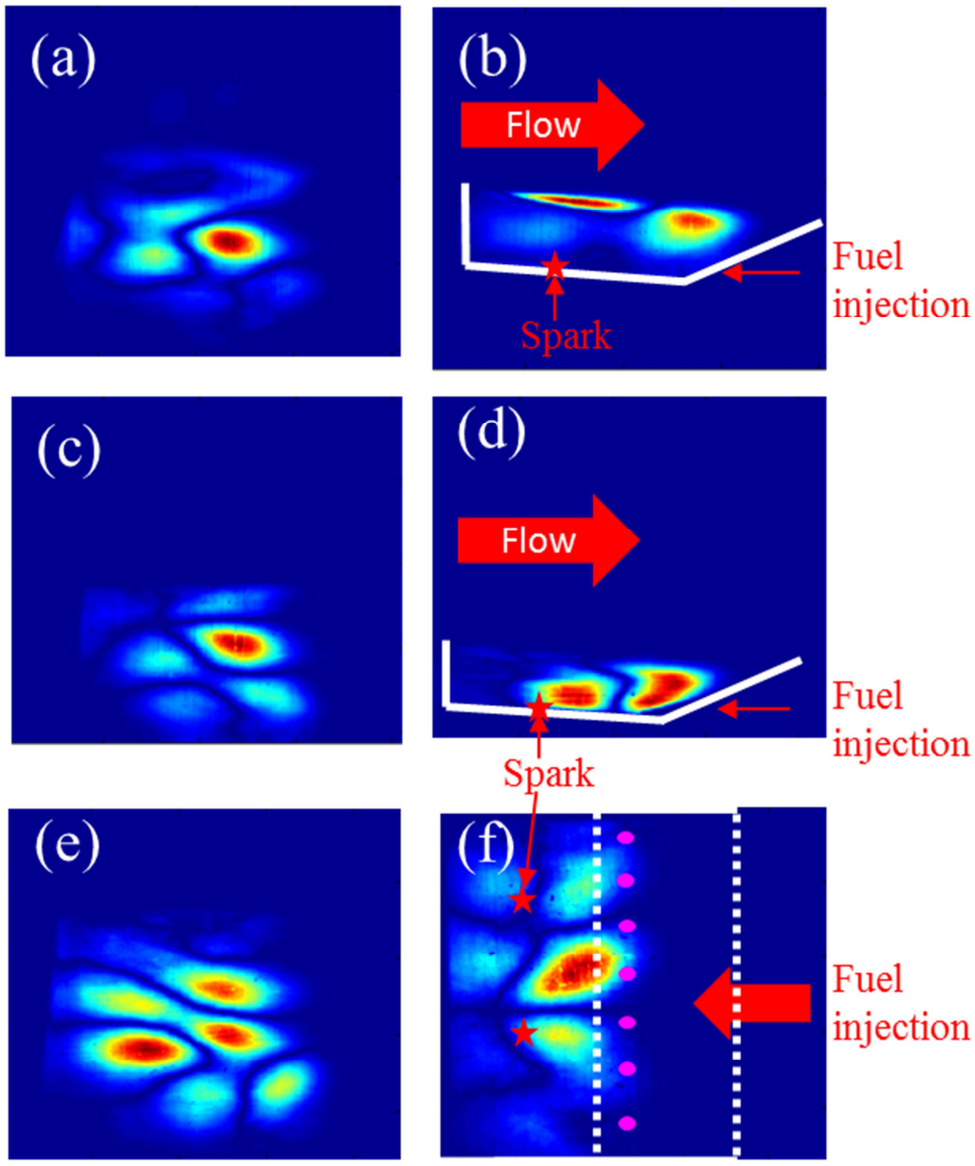

Figure 4.8. Second eigenmode of fuel-lean flame.

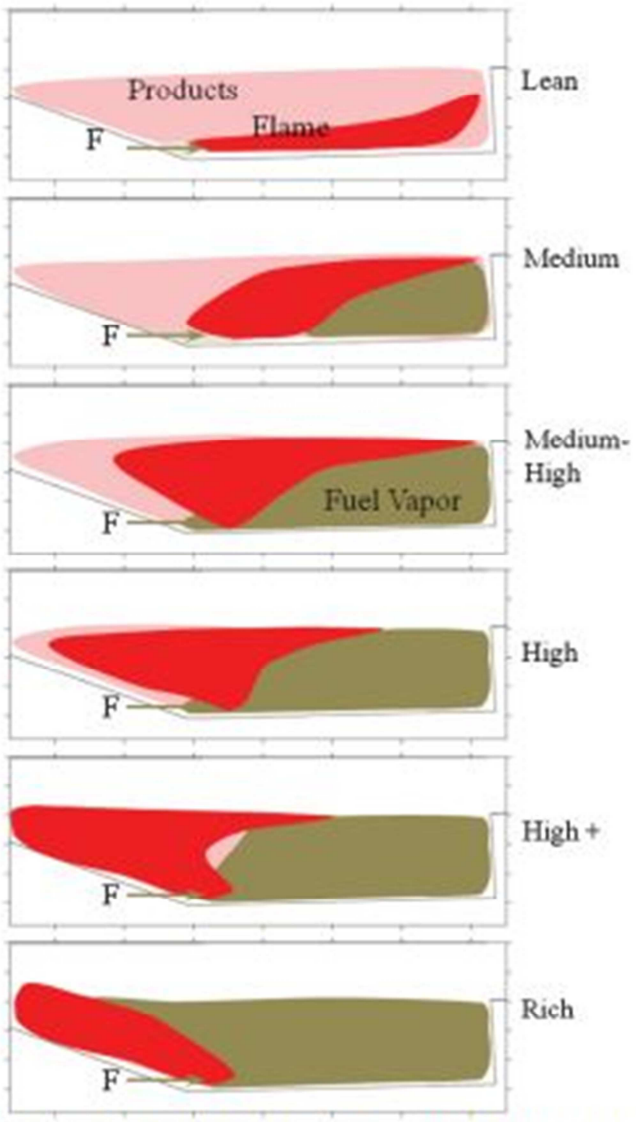

Figure 4.9. Diagram of heat release, combustion products and fuel vapor with increasing fuel flow rates [118].

This is indicative in every panel of the comparison between Figure 4.7 and Figure 4.8, but most clearly in Panel (*f)* (top view). The center portion of the reaction zone has shifted slightly aft, whereas the wings (or flame structures closest to the combustor walls) drastically move downstream. This is also easily observed in a side-by-side comparison between instantaneous images of the top view FBE as well.

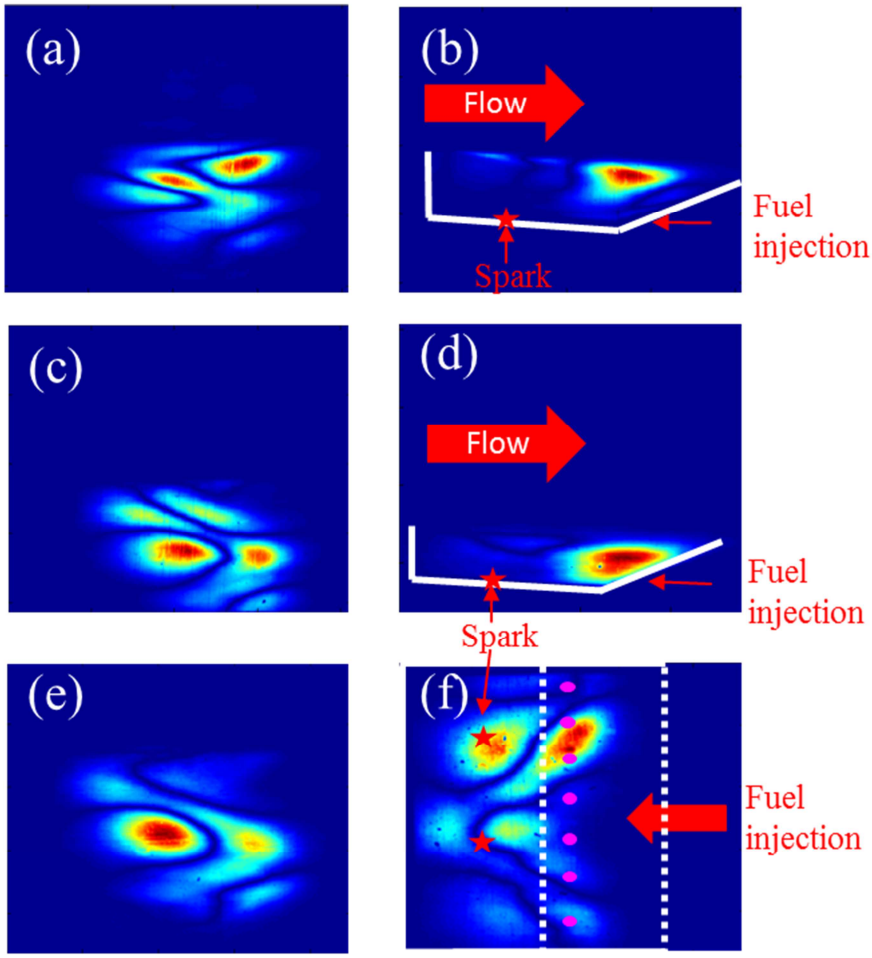

Figure 4.10. Second eigenmode of fuel-rich flame.

The last conclusion observed from the spatial eigenmodes was the change in flame shape as the fuel loading was increased. Directly comparing Panels (*c)* and (*e)* in **Error! Reference source not found.**Figure 4.5 for fuel-lean conditions to Figure 4.6 for fuel-rich conditions, a clear change in structure is evident. The flame structure appears more uniform and linear in the fuel-lean condition, but then changes into a nonlinear structure resembling an 'S' or an 'M' depending on the viewing angle for the fuel-rich condition. This nonlinear structure was observed to persist for periods of time during stable combustion and then dissipate, oscillating between the two modes. This could be indicative of a closed-loop thermo-acoustic disturbance, where the heat release couples

with the acoustical field fluctuations, but more information is needed via synchronized pressure measurements to validate this claim.

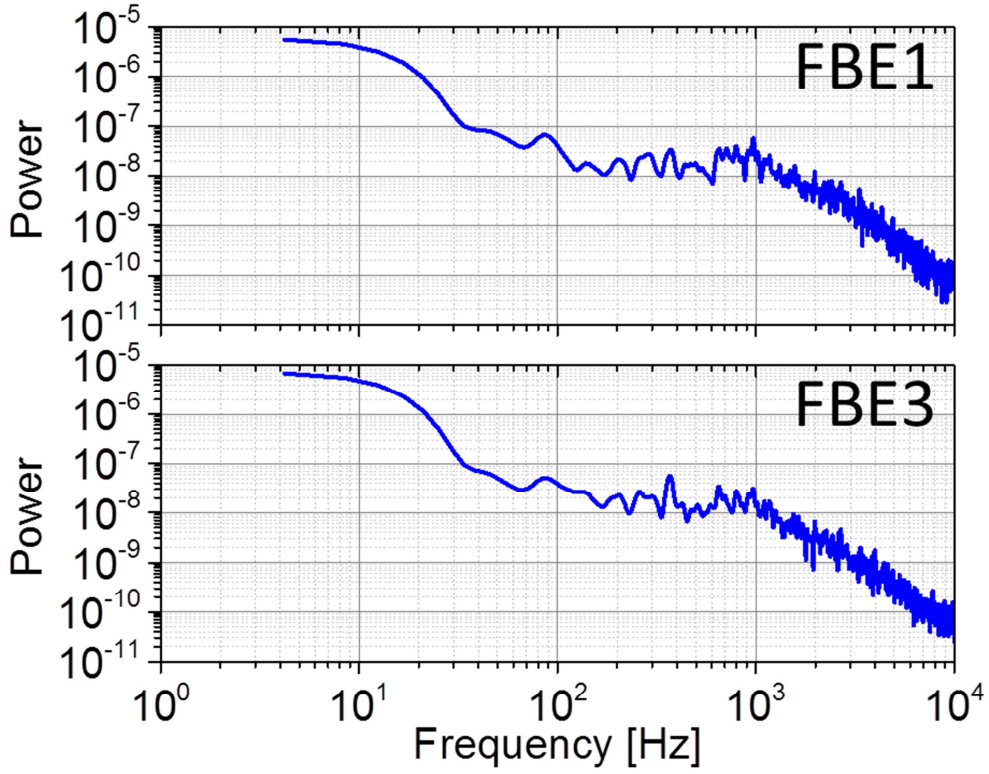

Figure 4.11. Power spectrum of fuel-lean conditions from FBE1 (top panel) and FBE3 (bottom panel).

Analyzing the power spectrum of the dominant temporal coefficients in the POD analysis also yielded some insight into the behavior of the cavity-based flame. First, it was observed that the power spectrum obtained was less sensitive to the particular viewing angle as compared to the spatial eigenmodes themselves. For example, when the temporal coefficients (a_1) associated with the first eigenmode were processed with a Fast Fourier Transform (FFT), the resulting power spectral densities from differing FBEs were quantitatively similar. Figure 4.11 shows the power spectral densities of FBE1 and FBE3, corresponding to angles 17.8 and 0.0 degrees, respectively for the fuel-lean case. The

images were taken at a frame rate of 20 kilo-Hertz (kHz); therefore, the single-sided amplitude spectrum could resolve frequencies up to 10 kHz. There appears to be no clear indication of a characteristic frequency, but the spectra still appear quantitatively similar.

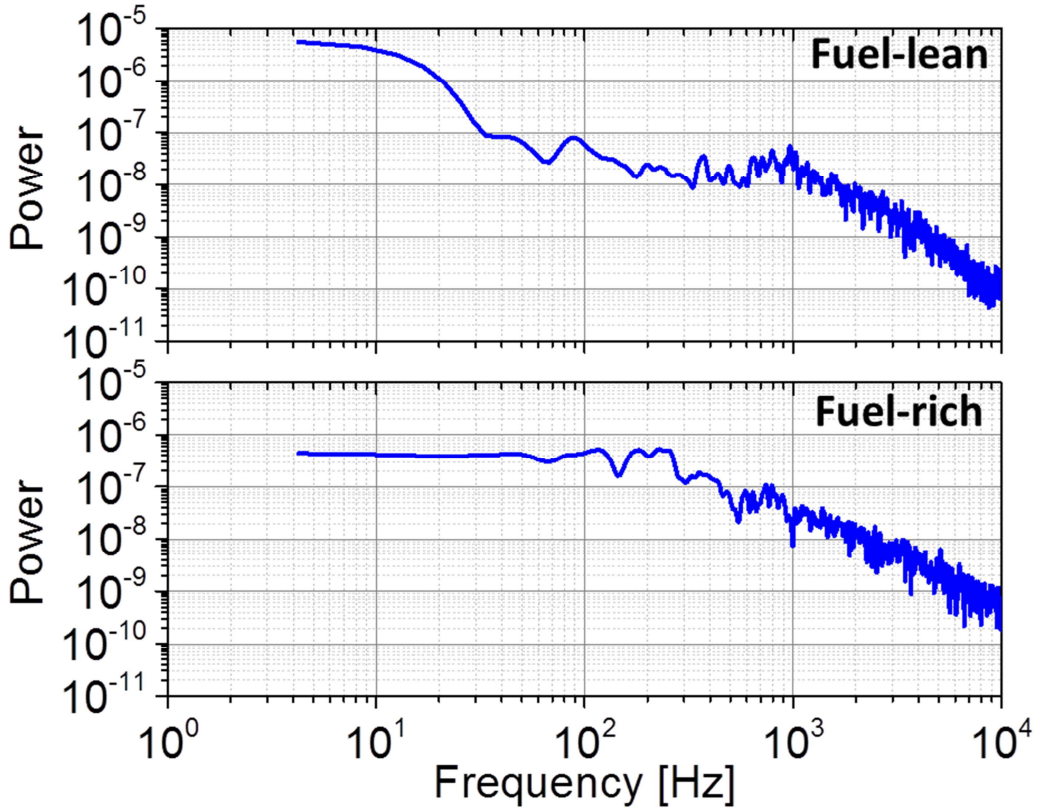

Figure 4.12. Power spectrum of FBE 8 for fuel-lean (upper) and fuel-rich (lower) conditions.

Second, it was observed that the power spectral densities differed as the fuel-loading changed. The a_1 temporal coefficients were again processed with an FFT, but for differing fuel cases and identical FBEs. Figure 4.12**Error! Reference source not found.** shows the power spectrum of FBE 8 for the fuel-lean case compared to the fuel-rich case. The spectra are qualitatively and quantitatively different. This relationship has been previously observed in subsonic and supersonic combustion with vee-gutter, blunt-body

combustion and the same geometry combustor as shown in this work, respectively [36, 37, 119].

The last conclusion drawn from analyzing the temporal coefficients was the temporal fluctuation of the $a_1(t)$ coefficient observed during the beginning stages of the ignition process. As described above, the cavity was initially ignited by 2 spark plugs, arcing for a duration of approximately 0.41 ms. "Stable" combustion was assumed to proceed directly after the spark plugs were turned off; however as observed in Figure 4.13, this appears not to be the case for the fuel-lean condition.

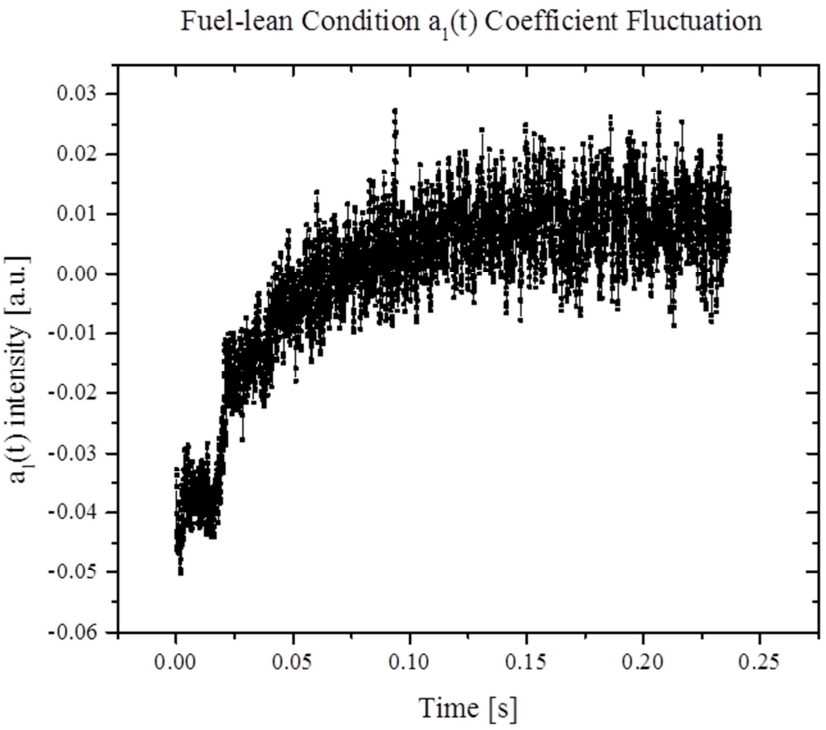

Figure 4.13. $a_1(t)$ intensity fluctuation of Frame b during fuel-lean testing conditions.

Figure 4.13 represents the $a_1(t)$ temporal coefficient for the entire temporal domain of the fuel-lean testing condition. Since the first eigenmode is the most energetic (44.3% relative energy), we can readily assume that the behavior of $a_1(t)$ accurately describes

the temporal evolution of the cavity combustion. Therefore, if the chemical reaction was indeed stable, the fluctuation should be relatively centered on the same mean. Instead, there appears to be a sharp increase in intensity at ~0.025 s, followed by a logarithmic increase until 0.125 s and then apparent "stable" combustion after that. Selective time intervals were chosen based on the intensity progression shown in Figure 4.13. The resulting instantaneous snapshots from FBE3 (0 degrees) is shown in Figure 4.14.

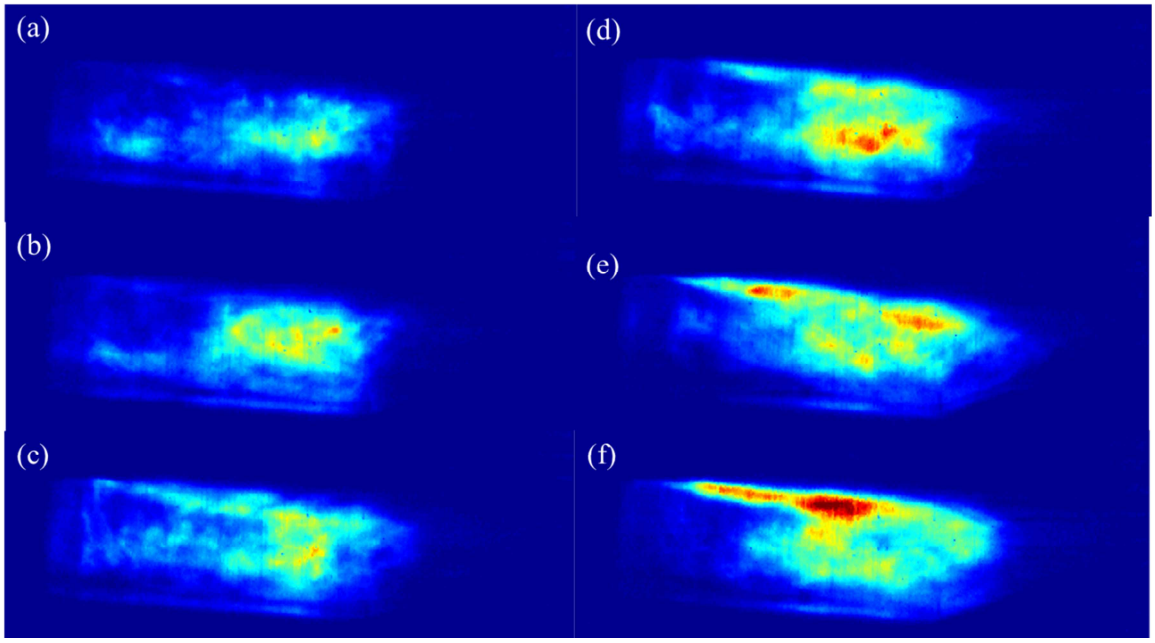

Figure 4.14. Fuel-lean FBE3 instantaneous snapshots at the following time selections (a). 0.01 s (b). 0.02 s (c). 0.0265 s (d). 0.03 s (e.) 0.04 s (f.) 0.225 s

One possible explanation for this behavior is for these operating conditions, the combustion reaction does not stabilize until approximately 113 ms after the first kernel was observed in the cavity. Moreover, during this "ignition" period the flame structures changed with time from an intense burning zone near the closeout ramp (Panel *a* in Figure 4.14) to a shear-layer flame anchored on the leading edge of the cavity (Panel *f* Figure 4.14). This phenomenon can be explained due to a thermal effect within the

cavity. For example, upon initial ignition the upstream cavity section/leading edge is too cold to anchor the flame, but as the cavity heats up due to heat transfer from sustained combustion, the flame then anchors in the shear layer.

The POD calculation was repeated using different segments of images (ie: 262-5,000, 1,000-5,000, 3,000-5,000, etc), but the dominant eigenmode structure remained unchanged. However, the relative energy content decreased from 44.3% for eigenmode 1 using all frames to < 20% when only the last 2,000 frames were used. This is due to the nature of POD, as explained above, where it excels at capturing the large scale structures in flow fields, but is weak at capturing individualistic events like this process is. The dominant structure within this cavity is a shear-layer based flame, which is evident in first eigenmode shown in Figure 4.5.

4.3. Fourier and Wavelet Analysis

A Fourier analysis was completed on all of the projections for both the fuel conditions specified in Table 4.1. The spatial fluctuations for the fuel-lean condition resembled the same structure as observed with the $a_1(t)$ temporal coefficient in the previous section, as shown in Figure 4.15. However, the chaotic nature of the fluctuation yielded no characteristic frequencies in any of the perspectives at this time. An example of the Fourier analysis for the *x* and *y* centroid for FBE3 during fuel-lean combustion is shown in Figure 4.16.

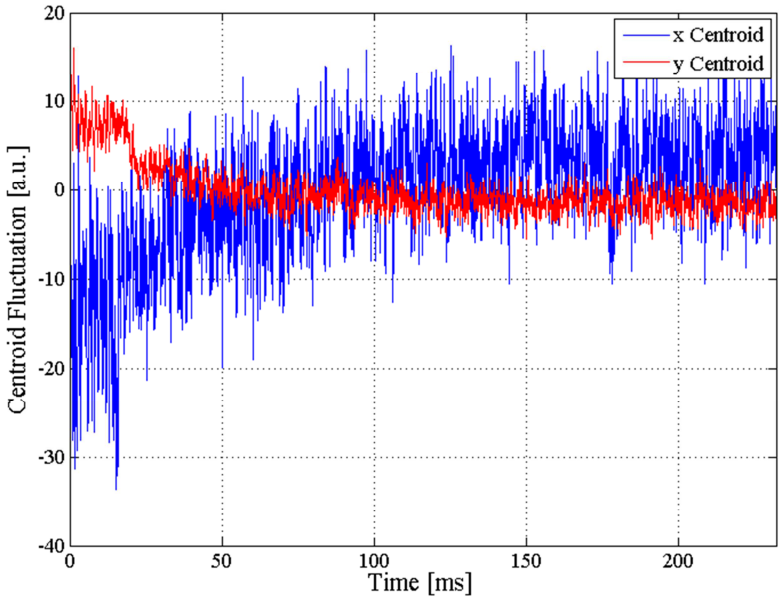

Figure 4.15. Fuel-lean FBE3 x and y centroid spatial fluctuation.

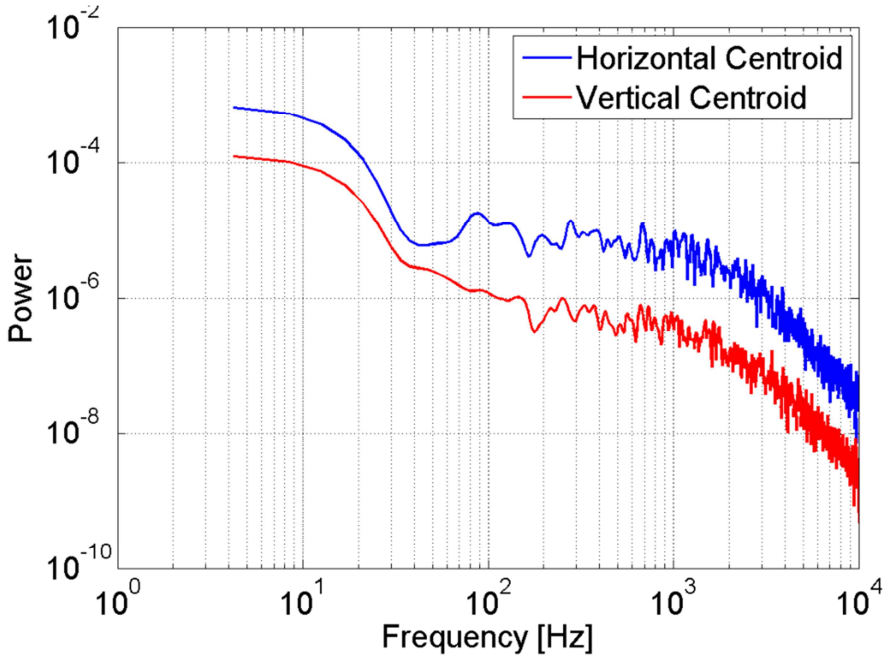

Figure 4.16. Power spectral density of x and y centroid fluctions from FBE3 during fuel-lean conditions.

More diagnostic tests are needed along with more analysis to characterize the ignition process, so that different intervals can be processed independently for more meaningful characteristic frequency results.

A wavelet analysis was also applied to each chemiluminescence perspective. An example of the $a_1(t)$ coefficients for FBE3, processed with a CWT are shown in Figure 4.17 as a function of fuel-loading condition.

.

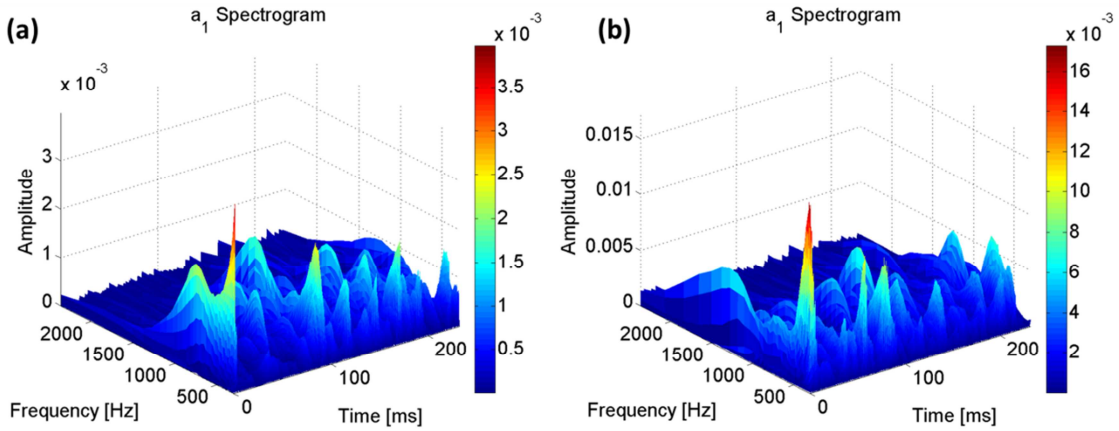

Figure 4.17. CWT of $a_1(t)$ temporal coefficients for FBE3 under (a). fuel-lean conditions (b). fuel-rich conditions.

The WA accurately captures the dynamics present in the data, as previously discussed in Chapter 3 and indicative of the high amplitude peak at ~0.025 s, but as with the Fourier analysis, more information is needed in order to accurately extract useful information from these figures. Another comparable example of the WA is shown in Figure 4.18 corresponding to FBE7 (top view).

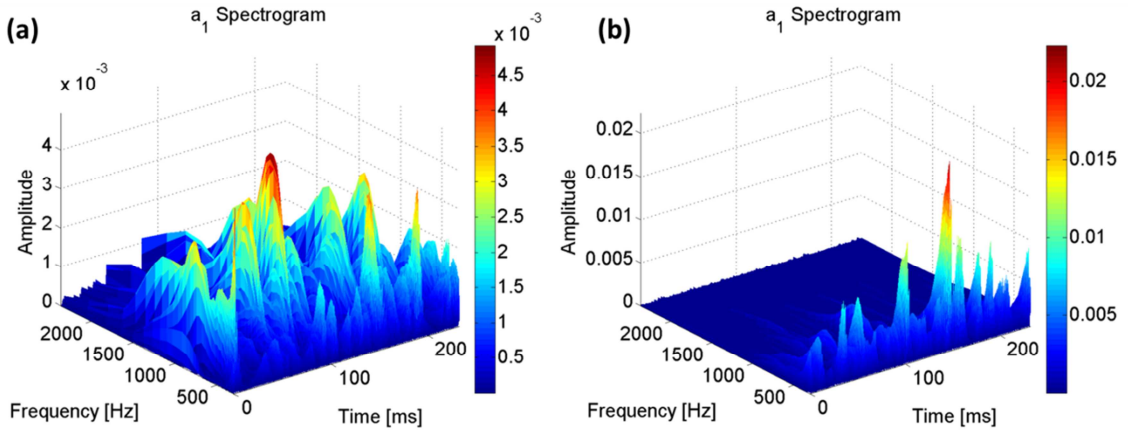

Figure 4.18. CWT of $a_1(t)$ temporal coefficients for FBE7 under (a). fuel-lean conditions (b). fuel-rich conditions.

4.4. Summary

A cavity-based flameholder fueled from the closeout ramp was characterized using multiple perspective chemiluminescence at Mach 2 inlet conditions. These data were combined with previously obtained particle image velocimetry to understand the interplay between combustion and the flow field. The multiple perspective chemiluminescence was possible using two 4×1 optical fiber bundles coupled with high-speed cameras, which yielded seven total perspectives in this experiment due to one fiber not being used.

Analysis of the data measured at 20 kHz for a duration of 0.25 seconds per condition using proper orthogonal decomposition in combination with a fast Fourier transform yield the following major observations.

1. The dominant eigenmode structures differed depending on the FBE perspective, which is indicative of the 3D composition of the flame front.

2. These dominant structures were confirmed from various perspectives to embody non-uniform features that would shift farther downstream with increasing fuel rates as indicated by previous studies.
3. The power spectrum obtained from the temporal coefficients associated with the dominant eigenmodes was less sensitive to the particular viewing registration when compared to the eigenmodes themselves.
4. The power spectra obtained from the same temporal coefficients differed as a function of fuel flow rate, as observed from previous studies.

Chapter 5. Conclusions and future work

This chapter summarizes the principal findings and conclusions derived from this dissertation, and provides some recommendations for future work.

5.1. Conclusions

In summary, this work focused on the development of advanced diagnostics and the corresponding analysis algorithms for high speed flows. A new diagnostic capability was developed by combining chemiluminescence imaging with FBEs, and was demonstrated in a Mach 2 combustor to enable imaging measurements from eight perspectives simultaneously at a 20 kHz repetition rate. Spatially, such measurements provide full-field information of the flow and combustion processes; and temporally, such measurements are sufficient to resolve many of the governing processes under such challenging flow conditions. The high speed and multi-perspective nature of such a diagnostic capability calls for algorithms that can process large datasets and extract key physics effectively. Therefore, this work also investigated several algorithms, including the Fourier transform, proper orthogonal decomposition, and wavelet transform. These algorithms were first tested on single-perspective measurements obtained in a subsonic flow, demonstrating their ability to extract key flow and combustion parameters. After these relatively simple tests, these algorithms were applied to the multi-perspective measurements obtained in the supersonic flows to reveal the dominant flow structures.

The first chapter describes the motivations for this thesis and lays the groundwork for the independent analysis of characteristic frequencies associated with the dominant

unsteady heat release modes for a subsonic vee-gutter model afterburner and a supersonic model ramjet combustor.

The second chapter describes the fundamental principles of the various components relevant to this dissertation due to multi-physics nature of the work. First, combustion instabilities and how they can be detrimental to combustion efficiency and engine design. Then this chapter also outlines how these combustion instabilities present themselves in subsonic combustion and supersonic combustion flows, which highlights the need to investigate the spatial structure and dominant oscillatory modes inherent with unsteady heat release in order to gain insight for improved physical understanding. This chapter then explains the fundamentals of chemiluminescence measurements. Lastly, this chapter provides an example of monitoring heat release modes via the combined use of CH* chemiluminescence and various mathematical analysis tools (including proper orthogonal decomposition and continuous wavelet transform).

The third chapter applies the aforementioned chemiluminescence diagnostics and numerical methods to a subsonic combustor with a vee-gutter flameholder for steady and unsteady combustion. The stable results indicated that the flame area within the measurement volume decreased when the Mach number was increased from 0.15 to 0.20 at stoichiometric conditions. This was indicated by thinner flame sheets on either side of the vee-gutter center line and a greater distance between dominant oscillatory modes, as revealed by the proper orthogonal decomposition analysis. Overall, this increase in Mach number yielded a flame structure that was more stable, due to the decreased unsteady heat release fluctuation observed in the wavelet analysis. The unstable results indicated that the continuous wavelet transform analysis yielded more conclusive characteristic

frequencies than the Fourier or POD analysis, due to its ability to characterize a local time-frequency relationship versus a global one as with a Fourier transform.

The fourth chapter applies the chemiluminescence diagnostics and numerical analysis to a supersonic combustor with a cavity-based flameholder. The measurements were performed at 20 kHz for steady combustion under two fuel flow rates. With the help of fiber-based endoscopes, multi-perspective measurements were obtained and used in the study. This is the first time that multi-perspective measurements have been obtained on a supersonic combustor at a 20 kHz rate. The results captured a 3D flame structure that was not axisymmetric as expected. Previous hypotheses proposed for this combustor geometry were also confirmed by visually observing the multi-perspective measurements. For example, a downstream shift in flame structure occurs with increasing fuel-flow rates. Cold regions, lacking in combustion, were also observed on either side of the cavity centerline, indicative of fuel-rich lobes leading to very poor combustion in the upstream end of the cavity coupled with non-uniform burning in the downstream portion of the cavity. The imaging was observed on such a fast temporal scale that the ignition processes of the combustor can be resolved, showing each structure corresponding to each phase of the startup process. However, more diagnostic efforts (such as three-dimensional reconstruction) need to be completed in order to characterize this process in depth to yield more significant results.

5.2 Future work

Lastly, based on the work described in this dissertation, the following research areas are identified and recommended for further investigation.

First, the multiple perspective chemiluminescence images could be used to obtain 3D flame structures via tomographic inversion similar to the approaches demonstrated by Li et al. [120] and Cai et al. [112]. This would enable new possibilities for model validation and model development. For example, a reactive LES solution could be calculated as in Roux [121] and the iso-surface of flame fronts obtained numerically could be compared directly to the experimentally measured one. Also, 2D, line-of-sight, chemiluminescence averages could be calculated numerically, as shown in Blanchard [23], that correspond to the individual viewing projections of each FBE for a reduced order validation. Both comparisons could be completed with minimal optical access experimentally to improve meshing and solution strategies for CFD and LES simulations, even for complex combustor geometries.

Second, a Mie scattering measurements could be performed simultaneously with the CH* chemiluminescence measurements for cross-comparison and cross-validation purposes. Such experiments should be further examined and applied to turbulent and/or bluff-body flames. Preliminary efforts on laminar flames, not reported in this thesis, were promising, but there was difficulty in accurately capturing the flame edge using existing algorithms for turbulent flames. An algorithm similar to Qiu et al. [122, 123] should be explored to facilitate this process. Accurate representation of this inner, thermal, flame structure in comparison to the chemically excited, outer, flame structure could be valuable for chemical reaction models and analytic models, where the flame sheet is often assumed as infinitesimally thin [124, 125]. Also, the planar Mie scattering measurements could be used to validate the 3D tomographic reconstruction, by direct comparison between the planar Mie scattering against a 2D slice of the 3D reconstruction. Such a

comparison will directly validate the 3D tomographic reconstruction, and also provides insights to the limitations and capabilities of both Mie scattering and chemiluminescence diagnostics for flame measurements.

Third, the POD combined with WA yielded interesting dynamics for vee-gutter combustion during LBO. More data should be captured using different inlet temperatures and different fuel compositions to further quantify these dynamics. This could lead to critical mode shapes that act as a precursor to LBO phenomena.

Fourth, the POD analysis of the supersonic combustion data revealed interesting dynamics for the ignition process that should be further examined. As mentioned in Chapter 4, steady-state combustion did not stabilize until about 113 ms into the test versus 13.1 ms reported in this thesis, based on the magnitudes of the dominant POD temporal coefficients. The difference in these values did not change the attributes of the modes shapes of the heat release, but there was an intensity change in the temporal coefficients indicative of an unsteady combustion. More diagnostics efforts should be pursued to quantify these "ignition" modes to help with the combustion understanding of scramjet combustors.

Lastly, after researching the subsonic and supersonic combustors independently, more work should be completed to bridge the gap between the subsonic (Mach 0.20) and supersonic (Mach 2) conditions reported in this thesis. Upon further analysis, the flame speed within the scramjet's cavity was found to be in the range of 100-200 m/s depending on condition. This does not quite compare to the flame speed of the vee-gutter model afterburner, which was in the range of 70-92 m/s depending on condition. The CSDL at Virginia Tech did not have the capabilities to preheat the vee-gutter combustor to

anything higher than 600 degrees Fahrenheit nor have the compressor power to operate a continuous air flow of greater than 1000 scfm, as shown in Figure 3.2. The highest light off condition tested at the CSDL was Mach 0.225 (102 m/s flame speed) with a corresponding inlet temperature of 460 degrees Fahrenheit, but the compressor was not able to sustain this under stable conditions for further analysis. Therefore, it is suggested to increase the capabilities of the CSDL to expand the testing envelope of the vee-gutter rig to analyze flame structures in the 100-200 m/s range. This would be attainable if the preheating capabilities were doubled (300 kW electric heating) and the compressor capabilities were increased to allow for at least 1300 scfm of air. This would facilitate 1). the analysis of vee-gutter combustion at more realistic afterburning conditions and 2). allow for the comparison of flame structure and heat release characteristic frequencies to other flameholder designs, such as the scramjet cavity-based one analyzed in this thesis.

References

1. T. C. Lieuwen, V. Yang, and F. K. Lu, *Combustion instabilities in gas turbine engines: operational experience, fundamental mechanisms and modeling* American Institute of Aeronautics and Astronautics, (2005).
2. T. C. Lieuwen, *Unsteady combustor physics* (Cambridge University Press, 2012).
3. D. Veynante, and L. Vervisch, "Turbulent combustion modeling," Progress in Energy and Combustion Science **28**, 193-266 (2002).
4. H. Pitsch, "Large-eddy simulation of turbulent combustion," Annu. Rev. Fluid Mech. **38**, 453-482 (2006).
5. K. T. Kim, *Forced response on swirl stabilized flames in hydrogen enriched gas turbines* (The Pennsylvania State University, 2009).
6. J. Lee, and D. Santavicca, "Experimental diagnostics for the study of combustion instabilities in lean premixed combustors," Journal of propulsion and power **19**, 735-750 (2003).
7. S. Candel, "Combustion dynamics and control: Progress and challenges," Proceedings of the Combustion Institute **29**, 1-28 (2002).
8. D. Kim, J. G. Lee, B. D. Quay, D. A. Santavicca, K. Kim, and S. Srinivasan, "Effect of flame structure on the flame transfer function in a premixed gas turbine combustor," Journal of Engineering for Gas Turbines and Power **132**, 021502 (2010).
9. J. G. Lee, K. Kim, and D. Santavicca, "Measurement of equivalence ratio fluctuation and its effect on heat release during unstable combustion," Proceedings of the Combustion Institute **28**, 415-421 (2000).
10. T. Lieuwen, and B. T. Zinn, "The role of equivalence ratio oscillations in driving combustion instabilities in low NO_x gas turbines," in *Symposium (International) on Combustion*, pp. 1809-1816.
11. J. H. Cho, and T. Lieuwen, "Laminar premixed flame response to equivalence ratio oscillations," Combustion and Flame **140**, 116-129 (2005).
12. P. M. Allison, Y. Chen, M. Ihme, and J. F. Driscoll, "Coupling of flame geometry and combustion instabilities based on kilohertz formaldehyde PLIF measurements," Proceedings of the Combustion Institute (2014).
13. R. Blanchard, A. Wickersham, L. Ma, W. Ng, and U. Vandsburger, "Simulating Bluff-Body Flameholders: On the Use of Proper Orthogonal Decomposition for Combustion Dynamics Validation," Journal of Engineering for Gas Turbines and Power **136**, 121504-121501 (2014).
14. S. Chaudhuri, and B. M. Cetegen, "Blowoff characteristics of bluff-body stabilized conical premixed flames with upstream spatial mixture gradients and velocity oscillations," Combustion and flame **153**, 616-633 (2008).

15. B. Kiel, K. Garwick, J. R. Gord, J. Miller, A. Lynch, R. Hill, and S. Phillips, "A detailed investigation of bluff body stabilized flames," in *45th AIAA Aerospace Sciences Meeting & Exhibit* (2007), pp. 2007-2168.

16. S. Kheirkhah, and Ö. Gülder, "Turbulent premixed combustion in V-shaped flames: Characteristics of flame front," Physics of Fluids (1994-present) **25**, 055107 (2013).

17. J. Longwell, "Flame stabilization by bluff bodies and turbulent flames in ducts," in *Symposium (International) on Combustion,* Vol. 4, No. 1, pp 90-97 (1953).

18. B. Emerson, J. Lundrigan, J. O'Connor, D. Noble, and T. Lieuwen, "Dependence of the bluff body wake structure on flame temperature ratio," in *49th AIAA Aerospace Sciences Meeting including the New Horizons Forum and Aerospace Exposition* (2011).

19. F. H. Wright, and E. E. Zukoski, "Flame spreading from bluff-body flameholders," in *Symposium (International) on Combustion* Vol. 8, No. 1, pp. 933-943 (1961).

20. T. Maxworthy, "On the mechanism of bluff body flame stabilization at low velocities," Combustion and Flame **6**, 233-244 (1962).

21. S. J. Shanbhogue, S. Husain, and T. Lieuwen, "Lean blowoff of bluff body stabilized flames: Scaling and dynamics," Progress in Energy and Combustion Science **35**, 98-120 (2009).

22. R. Blanchard, A. Wickersham, L. Ma, W. Ng, and U. Vandsburger, "Simulating Bluff-body Flameholders: On the Use of Proper Orthogonal Decomposition for Combustion Dynamics Validation," Journal of Engineering for Gas Turbines and Power **136**, 121504-121501 (2014).

23. R. P. Blanchard, "Simulating Bluff-body Flameholders: On the Use of Proper Orthogonal Decomposition for Combustion Dynamics Validation," (Virginia Polytechnic Institute and State University, 2014).

24. J. Song, C. Jung, J. Hwang, and Y. Yoon, "An Experimental Study on the Flame Dynamics with V-Gutter Typer Flameholder in the Model Combustor," AIAA 2011 **6126** (2011).

25. M. Macquisten, and A. Dowling, "Low-frequency combustion oscillations in a model afterburner," Combustion and Flame **94**, 253-264 (1993).

26. T. Schuller, D. Durox, and S. Candel, "A unified model for the prediction of laminar flame transfer functions: comparisons between conical and V-flame dynamics," Combustion and Flame **134**, 21-34 (2003).

27. S. Kato, T. Fujimori, A. Dowling, and H. Kobayashi, "Effect of heat release distribution on combustion oscillation," Proceedings of the Combustion Institute **30**, 1799-1806 (2005).

28. Shreekrishna, S. Hemchandra, and T. Lieuwen, "Premixed flame response to equivalence ratio perturbations," Combustion Theory and Modelling **14**, 681-714 (2010).

29. A. Ben-Yakar, and R. K. Hanson, "Cavity flame-holders for ignition and flame stabilization in scramjets: An overview," J. Propul. Power **17**, 869-877 (2001).

30. M. R. Gruber, J. M. Donbar, C. D. Carter, and K.-Y. Hsu, "Mixing and combustion studies using cavity-based flameholders in a supersonic flow," J. Propul. Power **20**, 769-778 (2004).

31. M. R. Gruber, R. A. Baurle, T. Mathur, and K. Y. Hsu, "Fundamental studies of cavity-based flameholder concepts for supersonic combustors," J. Propul. Power **17**, 146-153 (2001).

32. S. D. Hammack, T. Lee, K.-Y. Hsu, and C. D. Carter, "High-Repetition-Rate OH Planar Laser-Induced Fluorescence of a Cavity Flameholder," J. Propul. Power **29**, 1248-1251 (2013).

33. C. C. Rasmussen, J. F. Driscoll, K. Y. Hsu, J. M. Donbar, M. R. Gruber, and C. D. Carter, "Stability limits of cavity-stabilized flames in supersonic flow," Proceedings of the Combustion Institute **30**, 2825-2833 (2005).

34. K.-C. Lin, C.-J. Tam, I. Boxx, C. Carter, K. Jackson, and M. Lindsey, "Flame characteristics and fuel entrainment inside a cavity flame holder in a scramjet combustor," AIAA Paper **5381**, 2007 (2007).

35. J.-Y. Choi, F. Ma, and V. Yang, "Combustion oscillations in a scramjet engine combustor with transverse fuel injection," Proceedings of the Combustion Institute **30**, 2851-2858 (2005).

36. F. Ma, J. Li, V. Yang, K.-C. Lin, and T. A. Jackson, "Thermoacoustic flow instability in a scramjet combustor," AIAA Paper **3824**, 2005 (2005).

37. K.-C. Lin, K. Jackson, R. Behdadnia, T. A. Jackson, F. Ma, and V. Yang, "Acoustic Characterization of an Ethylene-Fueled Scramjet Combustor with a Cavity Flameholder," Journal of Propulsion and Power **26**, 1161-1169 (2010).

38. C. C. Rasmussen, J. F. Driscoll, C. D. Carter, and K. Y. Hsu, "Characteristics of cavity-stabilized flames in a supersonic flow," J. Propul. Power **21**, 765-768 (2005).

39. W. H. A. Jr., "Fuel-Air Injection Effects on Combustion in Cavity-Based Flameholders in a Supersonic Flow," in *Aeronautics and Astronautics*(Air Force Institute of Technology, 2005), p. 104.

40. K.-Y. Hsu, C. Carter, M. Gruber, T. Barhorst, and S. Smith, "Experimental study of cavity-strut combustion in supersonic flow," J. Propul. Power **26**, 1237-1246 (2010).

41. S. G. Tuttle, C. D. Carter, and K.-Y. Hsu, "Particle Image Velocimetry in a Nonreacting and Reacting High-Speed Cavity," Journal of Propulsion and Power **30**, 576-591 (2014).

42. C. C. Rasmussen, S. K. Dhanuka, and J. F. Driscoll, "Visualization of flameholding mechanisms in a supersonic combustor using PLIF," Proceedings of the Combustion Institute **31**, 2505-2512 (2007).

43. K. M. Kim, S. W. Baek, and C. Y. Han, "Numerical study on supersonic combustion with cavity-based fuel injection," International Journal of Heat and Mass Transfer **47**, 271-286 (2004).

44. D. M. Peterson, M. Hagenmaier, C. D. Carter, and S. G. Tuttle, "Hybrid Reynolds-Averaged and Large-Eddy Simulations of a Supersonic Cavity Flameholder," AIAA Paper **2483**, 2013 (2013).

45. A. G. Gaydon, H. G. Wolfhard, and S. Penner, "Flames, their structure, radiation and temperature," Journal of Applied Mechanics **27**, 600 (1960).

46. V. N. Nori, *Modeling and analysis of chemiluminescence sensing for syngas, methane and Jet-A combustion* (Georgia Institute of Technology, 2008).

47. J.-M. Samaniego, F. Egolfopoulos, and C. Bowman, "CO2* chemiluminescence in premixed flames," Combustion Science and Technology **109**, 183-203 (1995).

48. Y. Hardalupas, and M. Orain, "Local measurements of the time-dependent heat release rate and equivalence ratio using chemiluminescent emission from a flame," Combustion and Flame **139**, 188-207 (2004).

49. T. Kathrotia, U. Riedel, A. Seipel, K. Moshammer, and A. Brockhinke, "Experimental and numerical study of chemiluminescent species in low-pressure flames," Applied Physics B **107**, 571-584 (2012).

50. H. N. Najm, P. H. Paul, C. J. Mueller, and P. S. Wyckoff, "On the adequacy of certain experimental observables as measurements of flame burning rate," Combustion and Flame **113**, 312-332 (1998).

51. M. J. Bedard, S. V. Sardeshmukh, T. L. Fuller, W. E. Anderson, and M. Tanabe, "Chemiluminescence as a diagnostic in studying combustion instability in a practical combustor." AIAA (2014).

52. N. Docquier, and S. Candel, "Combustion control and sensors: A review," Progress in Energy and Combustion Science **28**, 107-150 (2002).

53. T. Muruganandam, B.-H. Kim, M. Morrell, V. Nori, M. Patel, B. Romig, and J. Seitzman, "Optical equivalence ratio sensors for gas turbine combustors," Proceedings of the Combustion Institute **30**, 1601-1609 (2005).

54. M. Yamazaki, M. Ohya, and K. Tsuchiya, "Detection of Air Equivalence Ratio of a Burner by Flame Emission-Spectrum," Kagaku Kogaku Ronbunshu **14**, 713-720 (1988).

55. C. Panoutsos, Y. Hardalupas, and A. Taylor, "Numerical evaluation of equivalence ratio measurement using OH* and CH* chemiluminescence in premixed and non-premixed methane–air flames," Combustion and Flame **156**, 273-291 (2009).

56. A. Sandrowitz, J. Cooke, and N. Glumac, "Flame emission spectroscopy for equivalence ratio monitoring," Applied spectroscopy **52**, 658-662 (1998).

57. M. Lauer, and T. Sattelmayer, "On the adequacy of chemiluminescence as a measure for heat release in turbulent flames with mixture gradients," Journal of Engineering for Gas Turbines and Power **132**, 061502 (2010).

58. B. Ayoola, R. Balachandran, J. Frank, E. Mastorakos, and C. Kaminski, "Spatially resolved heat release rate measurements in turbulent premixed flames," Combustion and Flame **144**, 1-16 (2006).

59. S. Farhat, W. Ng, and Y. Zhang, "Chemiluminescent emission measurement of a diffusion flame jet in a loudspeaker induced standing wave," Fuel **84**, 1760-1767 (2005).

60. T. Fiala, and T. Sattelmayer, "On the Use of OH* Radiation as a Marker for the Heat Release Rate in High-Pressure Hydrogen-Oxygen Liquid Rocket Combustion," 49th AIAA/ASME/SAE/ASEE Joint Propulsion Conference and Exhibit (2013).

61. T. Lieuwen, and Y. Neumeier, "Nonlinear pressure-heat release transfer function measurements in a premixed combustor," Proceedings of the combustion institute **29**, 99-105 (2002).

62. G. Bloxsidge, A. Dowling, and P. Langhorne, "Reheat buzz: an acoustically coupled combustion instability. Part 2. Theory," Journal of Fluid Mechanics **193**, 445-473 (1988).

63. M. Tamura, P. A. Berg, J. E. Harrington, J. Luque, J. B. Jeffries, G. P. Smith, and D. R. Crosley, "Collisional quenching of CH (A), OH (A), and NO (A) in low pressure hydrocarbon flames," Combustion and Flame **114**, 502-514 (1998).

64. V. N. Nori, and J. M. Seitzman, "CH* chemiluminescence modeling for combustion diagnostics," Proceedings of the combustion institute **32**, 895-903 (2009).

65. J. M. Hall, J. De Vries, A. R. Amadio, and E. L. Petersen, "Towards a kinetics model of CH chemiluminescence," AIAA paper **1318**, 43 (2005).

66. J. L. Lumley, "The structure of inhomogeneous turbulent flows," Atmospheric turbulence and radio wave propagation, 166-178 (1967).

67. S. V. Gordeyev, *Investigation of coherent structure in the similarity region of the planar turbulent jet using POD and wavelet analysis* (Harvard University, 1999).

68. D. Kosambi, "The estimation of map distances from recombination values," Annals of Eugenics **12**, 172-175 (1943).

69. K. Karhunen, *Zur spektraltheorie stochastischer prozesse* (Suomalainen tiedeakatemia, 1946).

70. M. Loève, *Probability Theory. Foundations. Random Sequences* (New York: D. Van Nostrand Company, 1955).

71. L. Sirovich, "Turbulence and the dynamics of coherent structures. I-Coherent structures. II-Symmetries and transformations. III-Dynamics and scaling," Quarterly of applied mathematics **45**, 561-571 (1987).

72. G. Berkooz, P. Holmes, and J. L. Lumley, "The proper orthogonal decomposition in the analysis of turbulent flows," Annual review of fluid mechanics **25**, 539-575 (1993).

73. L. Cordier, and T. Gilles, "Model Reduction, POD and Data Assimilation," in *Von Karman Institute*.

74. W. Cazemier, R. Verstappen, and A. Veldman, "Proper orthogonal decomposition and low-dimensional models for driven cavity flows," Physics of Fluids (1994-present) **10**, 1685-1699 (1998).

75. J. Pedersen, and K. Meyer, "POD analysis of flow structures in a scale model of a ventilated room," Experiments in Fluids **33**, 940-949 (2002).

76. T. Regert, P. Rambaud, and M. Reithmuller, "Investigation of the link between physics and POD modes," (DTIC Document, 2005).

77. B. Feeny, and R. Kappagantu, "On the physical interpretation of proper orthogonal modes in vibrations," Journal of Sound and Vibration **211**, 607-616 (1998).

78. A. Levey, and M. Lindenbaum, "Sequential Karhunen-Loeve basis extraction and its application to images," Image Processing, IEEE Transactions on **9**, 1371-1374 (2000).

79. I. Boxx, M. Stöhr, C. Carter, and W. Meier, "Temporally resolved planar measurements of transient phenomena in a partially pre-mixed swirl flame in a gas turbine model combustor," Combustion and Flame **157**, 1510-1525 (2010).

80. A. M. Steinberg, I. Boxx, M. Stöhr, C. D. Carter, and W. Meier, "Flow–flame interactions causing acoustically coupled heat release fluctuations in a thermo-acoustically unstable gas turbine model combustor," Combustion and Flame **157**, 2250-2266 (2010).

81. M. Stöhr, I. Boxx, C. D. Carter, and W. Meier, "Experimental study of vortex-flame interaction in a gas turbine model combustor," Combustion and Flame **159**, 2636-2649 (2012).

82. P. Iudiciani, C. Duwig, S. M. Hosseini, R. Szasz, L. Fuchs, E. Gutmark, A. Lantz, R. Collin, and M. Aldén, "Proper Orthogonal Decomposition for experimental investigation of swirling flame instabilities," in *48th AIAA Aerospace Sciences Meeting Including the New Horizons Forum and Aerospace Exposition, Orlando, USA* (2010), pp. 4-7.

83. F. Ichihashi, S.-M. Jeng, and K. Cohen, "Proper Orthogonal Decomposition and Fourier Analysis on the Energy Release Rate Dynamics of a Gas Turbine Combustor," in *48th AIAA Aerospace Science Meeting* (2010).

84. S. Kostka, A. C. Lynch, B. C. Huelskamp, B. V. Kiel, J. R. Gord, and S. Roy, "Characterization of flame-shedding behavior behind a bluff-body using proper orthogonal decomposition," Combustion and Flame **159**, 2872-2882 (2012).

85. P. Panda, M. Roa, and R. Lucht, "High Repetition Rate OH-PLIF of a Jet Flame in a Vitiated Swirling Crossflow and Qualitative Analysis using Proper Orthogonal Decomposition," (2014).

86. J.-D. Wu, and J.-C. Chen, "Continuous wavelet transform technique for fault signal diagnosis of internal combustion engines," NDT & E International **39**, 304-311 (2006).

87. C. Torrence, and G. P. Compo, "A Practical Guide to Wavelet Analysis," Bulletin of the American Meteorological Society **79**, 61-78 (1998).

88. M. Farge, "Wavelet transforms and their applications to turbulence," Annual review of fluid mechanics **24**, 395-458 (1992).

89. K. Schneider, and O. V. Vasilyev, "Wavelet methods in computational fluid dynamics*," Annual review of fluid mechanics **42**, 473 (2009).

90. W. Dahmen, "Wavelet and multiscale methods for operator equations," Acta numerica **6**, 55-228 (1997).

91. A. Cohen, and R. Masson, "Wavelet adaptive method for second order elliptic problems: Boundary conditions and domain decomposition," Numerische Mathematik **86**, 193-238 (2000).

92. K. Müller, G. Lohmann, S. Zysset, and D. Y. Von Cramon, "Wavelet statistics of functional MRI data and the general linear model," Journal of Magnetic Resonance Imaging **17**, 20-30 (2003).

93. R. Prosser, and R. Cant, "On the use of wavelets in computational combustion," Journal of Computational Physics **147**, 337-361 (1998).

94. A. K. Sen, G. Litak, R. Taccani, and R. Radu, "Wavelet analysis of cycle-to-cycle pressure variations in an internal combustion engine," Chaos, Solitons & Fractals **38**, 886-893 (2008).

95. Z. Wang, J. Ma, and M. Vo, "Recent progress in two-dimensional continuous wavelet transform technique for fringe pattern analysis," Optics and Lasers in Engineering **50**, 1052-1058 (2012).

96. J. Kastner, D. Cuppoletti, B. Malla, and E. Gutmark, "Optimization of Stochastic Estimation Techniques in a High-Speed, Axisymmetric Jet," in *48th AIAA Aerospace Sciences Meeting* (2010).

97. J. Kastner, B. Malla, E. Gutmark, J. Liu, and K. Kailasanath, "Using Wavelet Stochastic Estimation to correlate near-field pressure to velocity POD modes in a supersonic jet," AIAA paper (2012).

98. J. A. Ranalli, "Spatially resolved analysis of flame dynamics for the prediction of thermoacoustic combustion instabilities," (Virginia Polytechnic Institute and State University, 2009).

99. J. T. Farina, "Application of Multi-Port Mixing for Passive Suppression of Thermo-Acoustic Instabilities in Premixed Combustors," (Virginia Polytechnic Institute and State University, 2013).

100. P. Chatterjee, "A Computational Fluid Dynamics Investigation of Thermoacoustic Instabilities in Premixed Laminar and Turbulent Combustion Systems," (Virginia Polytechnic Institute and State University, 2004).

101. W. A. Chishty, "Effects of thermoacoustic oscillations on spray combustion dynamics with implications for lean direct injection systems," (Virginia Polytechnic Institute and State University, 2005).

102. A. G. Hendricks, "Determination of flame dynamics for unsteady combustion systems using tunable diode laser absorption spectroscopy," (Virginia Polytechnic Institute and State University, 2003).

103. R. Blanchard, A. Wickersham, I. Yeaton, C. Fleischman, S. Ekkad, W. Ng, U. Vandsburger, K. Lowe, and L. Ma, "Test Capabilities in the CCAPS/CSDL Augmentor Development Facility," in *51st AIAA Aerospace Sciences Meeting including the New Horizons Forum and Aerospace Exposition* (2013).

104. P. D. Welch, "The use of fast Fourier transform for the estimation of power spectra: a method based on time averaging over short, modified periodograms," IEEE Transactions on audio and electroacoustics **15**, 70-73 (1967).

105. T. Muruganandam, S. Nair, D. Scarborough, Y. Neumeier, J. Jagoda, T. Lieuwen, J. Seitzman, and B. Zinn, "Active control of lean blowout for turbine engine combustors," Journal of Propulsion and Power **21**, 807-814 (2005).

106. M. Gruber, and A. Nejad, "New supersonic combustion research facility," Journal of Propulsion and Power **11**, 1080-1083 (1995).

107. J. Ballester, and T. García-Armingol, "Diagnostic techniques for the monitoring and control of practical flames," Progress in Energy and Combustion Science **36**, 375-411 (2010).

108. H. Bheemul, G. Lu, and Y. Yan, "Three-dimensional visualization and quantitative characterization of gaseous flames," Measurement Science and Technology **13**, 1643 (2002).

109. L. Ma, S. Sanders, J. Jeffries, and R. Hanson, "Monitoring and control of a pulse detonation engine using a diode-laser fuel concentration and temperature sensor," Proceedings of the Combustion Institute **29**, 161-166 (2002).

110. L. Ma, W. W. Cai, X. Li, S. T. Sanders, A. W. Caswell, R. Sukesh, D. H. Plemmons, and J. R. Gord, "50 kHz rate 2D imaging of temperature and H2O concentration at exhaust plane of J85 engine by hyperspectral tomography," Optics Express (2012).

111. X. Li, and L. Ma, "Volumetric imaging of turbulent reactive flows at kHz based on computed tomography," Optics Express **22**, 4768-4778 (2014).

112. W. Cai, X. Li, F. Li, and L. Ma, "Numerical and experimental validation of a three-dimensional combustion diagnostic based on tomographic chemiluminescence," Optics express **21**, 7050-7064 (2013).

113. M. Kang, Y. Wu, and L. Ma, "Fiber-based endoscopes for 3D combustion measurements: view registration and spatial resolution," Combustion and Flame (2014).

114. M. M. Hossain, G. Lu, and Y. Yan, "Three-dimensional reconstruction of combustion flames through optical fiber sensing and CCD imaging," in *Instrumentation and Measurement Technology Conference (I2MTC), 2011 IEEE*(IEEE2011), pp. 1-5.

115. R. Dils, "High‐temperature optical fiber thermometer," Journal of Applied Physics **54**, 1198-1201 (1983).

116. J.-Y. Bouguet, "Camera calibration toolbox for matlab," (2004).

117. M. Kang, X. Li, and L. Ma, "Three-dimensional flame measurements using fiber-based endoscopes," Proceedings of the Combustion Institute (2014).

118. S. G. Tuttle, C. D. Carter, and K.-Y. Hsu, "Particle Image Velocimetry in an Isothermal and Exothermic High-Speed Cavity," in *50th AIAA Aerospace Sciences Meeting including the New Horizons Forum and Aerospace Exposition, AIAA*(2012).

119. A. J. Wickersham, X. Li, and L. Ma, "Advanced methods for extracting flow and combustion physics from high speed laser diagnostics," *AIAA Scitech* (2014).

120. X. Li, and L. Ma, "Three-Dimensional Measurements of Turbulent Jet Flames at kHz Rate Based on Tomographic Chemiluminescence," *AIAA Scitech* (2014).

121. S. Roux, G. Lartigue, T. Poinsot, U. Meier, and C. Bérat, "Studies of mean and unsteady flow in a swirled combustor using experiments, acoustic analysis, and large eddy simulations," Combustion and Flame **141**, 40-54 (2005).

122. T. Qiu, Y. Yan, and G. Lu, "A new edge detection algorithm for flame image processing," in *Instrumentation and Measurement Technology Conference (I2MTC), 2011 IEEE*(IEEE2011), pp. 1-4.

123. T. Qiu, Y. Yan, and G. Lu, "An autoadaptive edge-detection algorithm for flame and fire image processing," Instrumentation and Measurement, IEEE Transactions on **61**, 1486-1493 (2012).

124. T. Lieuwen, and K. McManus, "Introduction: combustion dynamics in lean-premixed prevaporized (LPP) gas turbines," Journal of Propulsion and Power **19**, 721-721 (2003).

125. V. Bellucci, B. Schuermans, D. Nowak, P. Flohr, and C. O. Paschereit, "Thermoacoustic modeling of a gas turbine combustor equipped with acoustic dampers," in *ASME Turbo Expo 2004: Power for Land, Sea, and Air* (American Society of Mechanical Engineers2004), pp. 635-644.